OXFORD

Cerebral Cortex, May 2018;28: 1625–1644

doi: 10.1093/cercor/bhx058
Advance Access Publication Date: 4 March 2017
Original Article

ORIGINAL ARTICLE

Mild Traumatic Brain Injury Induces Structural and Functional Disconnection of Local Neocortical Inhibitory Networks via Parvalbumin Interneuron Diffuse Axonal Injury

Michal Vascak, Xiaotao Jin, Kimberle M. Jacobs and John T. Povlishock

Department of Anatomy and Neurobiology, Virginia Commonwealth University Medical Center, PO Box 980709, Richmond, VA 23298-0709, USA

Address correspondence to John T. Povlishock, Department of Anatomy and Neurobiology, Virginia Commonwealth University Medical Center, Richmond, VA 23298-0709, USA. Email: john.povlishock@vcuhealth.org

Abstract

Diffuse axonal injury (DAI) plays a major role in cortical network dysfunction posited to cause excitatory/inhibitory imbalance after mild traumatic brain injury (mTBI). Current thought holds that white matter (WM) is uniquely vulnerable to DAI. However, clinically diagnosed mTBI is not always associated with WM DAI. This suggests an undetected neocortical pathophysiology, implicating GABAergic interneurons. To evaluate this possibility, we used mild central fluid percussion injury to generate DAI in mice with Cre-driven tdTomato labeling of parvalbumin (PV) interneurons. We followed tdTomato+ profiles using confocal and electron microscopy, together with patch-clamp analysis to probe for DAI-mediated neocortical GABAergic interneuron disruption. Within 3 h post-mTBI tdTomato+ perisomatic axonal injury (PSAI) was found across somatosensory layers 2–6. The DAI marker amyloid precursor protein colocalized with GAD67 immunoreactivity within tdTomato+ PSAI, representing the majority of GABAergic interneuron DAI. At 24 h post-mTBI, we used phospho-c-Jun, a surrogate DAI marker, for retrograde assessments of sustaining somas. Via this approach, we estimated DAI occurs in ~9% of total tdTomato+ interneurons, representing ~14% of pan-neuronal DAI. Patch-clamp recordings of tdTomato+ interneurons revealed decreased inhibitory transmission. Overall, these data show that PV interneuron DAI is a consistent and significant feature of experimental mTBI with important implications for cortical network dysfunction.

Key words: concussion, diffuse axonal injury, excitation/inhibition, fast-spiking, gray matter

Introduction

Traumatic brain injury (TBI) is a serious global healthcare problem (Langlois et al. 2006). Recent attention is on mild TBI (mTBI) that represents almost 90% of all TBIs (Cassidy et al. 2004; Mannix et al. 2016). Cognitive impairments are common sequelae of mTBI and extract a substantial toll on society (McAllister 1992; CDC 2003). Compared with moderate-to-severe TBI involving mass lesions, contusion, and overt cell death, mTBI pathology is undetectable using routine CT/MRI (Mittl et al. 1994; Povlishock and Katz 2005). However, converging evidence now suggests that more subtle structural and functional disconnection of cortical networks underlies cognitive impairment seen after mTBI (Sharp et al. 2014; Fagerholm et al. 2015; Wolf and Koch 2016).

Although mTBI pathophysiology remains unclear, it is now recognized that microscopic diffuse axonal injury (DAI) contributes to mTBI morbidity (Povlishock and Katz 2005; Johnson et al. 2013; Smith et al. 2013). Previously, we showed that DAI is

a progressive axonopathy leading to overt structural disconnection followed by widespread terminal loss and Wallerian degeneration (Povlishock et al. 1983; Erb and Povlishock 1991; Povlishock 1993; Christman et al. 1994). Although studying diffuse changes in the fine-scale structure of neocortex is difficult (Crick 1979; Povlishock and Christman 1995), emerging evidence supports that widespread terminal loss/deafferentation of cerebral networks contributes to mTBI morbidity and sets the stage for subsequent adaptive or maladaptive plasticity (Povlishock et al. 1992; Christman et al. 1997; Phillips and Reeves 2001; Huang et al. 2009; Marquez de la Plata et al. 2011; Patel et al. 2016; van der Horn et al. 2016). It has been assumed that this DAI elicits cortical network disconnection primarily via the white matter (WM) tracts' vulnerability for deformation (Adams et al. 1989, 1991). This belief arose primarily from human postmortem examinations (Strich 1956; Adams et al. 1982; Blumbergs et al. 1995) and was later reinforced with diffusion tensor imaging (DTI) of patients with TBI (Salmond et al. 2006; Bazarian et al. 2007; Kraus et al. 2007), which both revealed DAI signatures in the subcortical WM (SCWM), corpus callosum, and other deep WM tracts. While across the spectrum of TBI severity WM involvement cannot be dismissed (Mayer et al. 2010; Kinnunen et al. 2011), this presumption remains controversial in mTBI (Dodd et al. 2014). Several groups reported clinically diagnosed mTBI marked by substantial cognitive impairment without significant WM involvement (Zhang et al. 2010; Mac Donald et al. 2011; Ilvesmäki et al. 2014; Wäljas et al. 2014). This suggests an undetected structural–functional pathophysiology within neocortical gray matter (GM), where local (intrinsic) network processing relies on balanced excitatory/inhibitory neural activity (Aron 2007; Fries 2009; Haider and McCormick 2009; Raichle 2010). Supporting this possibility, studies measuring neocortical metabolic (functional MRI) and electromagnetic (electro- and magneto- encephalography) change, revealed a wide range of intrinsic neocortical network dysfunction involving abnormal spontaneous, rhythmic, and excitatory/inhibitory activity (Mayer et al. 2011; Sponheim et al. 2011; Tremblay et al. 2011; Bashir et al. 2012; De Beaumont et al. 2012; Luo et al. 2013; Huang et al. 2016; Palacios et al. 2017). Additionally, recent DTI studies of neocortical GM have detected reactive changes suggesting that mTBI disrupts local structural connectivity (Newcombe et al. 2011; Bouix et al. 2013; Ling et al. 2013). Collectively, these clinical findings strongly implicate that mTBI disrupts structural and functional connectivity in local neocortical networks formed by excitatory (glutamatergic) pyramidal neurons and inhibitory (GABAergic) interneurons (Somogyi et al. 1998; McCormick 2003; Douglas and Martin 2007).

Both clinical and experimental methodologies used to investigate neocortical GM excitatory/inhibitory networks have limitations. Advanced structural and functional neuroimaging in mTBI patients cannot resolve the specific neuronal and physiologic substrates of neocortical GM disruption (Logothetis 2008; Delouche et al. 2015). Further, in both human (Gentleman et al. 1993; Blumbergs et al. 1994; Sherriff et al. 1994) and animal investigations (Stone et al. 2000; Mac Donald et al. 2007) DAI is typically identified via amyloid precursor protein (APP) immunohistochemistry, which transiently accumulates at sites of impaired axonal transport following TBI (Maxwell et al. 1997; Smith et al. 2013). While APP+ accumulations (swellings) distal aspect demarcates the site of axonal disconnection (Greer et al. 2011; Wang et al. 2011), this strategy fails to provide retrograde information (e.g., glutamatergic vs. GABAergic) on the soma of origin (Büki et al. 2000; Povlishock and Stone 2001). Moreover, in the experimental setting excitatory/inhibitory neocortical network disruption has mostly been assessed in animal models that evoke cell death (Carron et al. 2016) and/or mass lesions involving neocortical contusion (Kobori and Dash 2006; Cantu et al. 2014; Hsieh et al. 2017), which typically do not occur in mTBI associated with DAI (Povlishock and Katz 2005; Parikh et al. 2007; Andriessen et al. 2010).

To critically address these issues, we developed a clinically relevant, well-controlled transgenic mouse model of mTBI uncomplicated by mass lesions/contusion and cell death (Greer et al. 2011). Exploiting cytosolic fluorescent protein expression, we conducted structural and functional assessments within neocortical GM of both DAI and non-DAI (intact) populations in a discrete subset (Thy1-expressing) of long-distance projecting excitatory pyramidal neurons. We reported that DAI within this pyramidal neuron subset primarily occurred near the soma of origin (Greer et al. 2013). We also found that this same perisomatic axonal injury (PSAI) was unresponsive to therapeutic targeting that proved neuroprotective within the underlying SCWM and corpus callosum (Hånell et al. 2015b). Importantly, these findings suggested DAI within neocortical GM vs. the underlying WM tracts involved different pathophysiological mechanisms. In concert with neocortical DAI we also observed widespread electrophysiological abnormalities among intact pyramidal neurons associated with local network hyperexcitability post-mTBI (Greer et al. 2012; Hånell et al. 2015a; Sun and Jacobs 2016). Since GABAergic interneurons regulate neocortical network activity (Isaacson and Scanziani 2011), these findings strongly implicated inhibitory interneuron disruption (Zhou et al. 2009; Yizhar et al. 2011; Lazarus et al. 2015).

While excitatory pyramidal neurons comprise 80% of neocortical neurons, their activity is controlled by the remaining 20% of inhibitory interneurons (DeFelipe and Fariñas 1992; Markram et al. 2004). The largest neocortical GABAergic interneuron subclass is genetically/molecularly characterized by parvalbumin (PV) expression and physiologically via their fast-spiking action potentials (Kawaguchi and Kubota 1997; Rudy et al. 2011). The extensive axonal arbor of a single PV+ interneuron can innervate up to a thousand neighboring postsynaptic neurons (Packer and Yuste 2011). In turn, PV+ interneurons receive converging inputs from excitatory pyramidal neurons and other PV+ interneurons (Gulyás et al. 1999), forming highly interconnected local neocortical networks that underlie gamma oscillations seen during cognitive loading (Howard 2003; Buzsáki and Wang 2012; Hu et al. 2014). Both clinical (Sponheim et al. 2011) and experimental (Paterno et al. 2016) mTBI studies have shown changes in these local neocortical firing patterns, which reflect changes in excitatory/inhibitory balance (Atallah and Scanziani 2009). Based on previous clinical observations, our own findings, and these PV+ interneuron properties, we questioned whether mTBI induces structural and functional disconnection via DAI within local neocortical inhibitory networks.

To address this issue, we further refined our mTBI model by employing Cre/lox mice (Madisen et al. 2010) to genetically label the total PV+ interneuron population (Hippenmeyer et al. 2005). Specifically, we relied on Cre-driven expression of the red fluorescent protein (RFP) tdTomato within PV+ interneurons, coupled with immunohistochemical strategies for optimal structural assessment of potential DAI via confocal and ultrastructural analysis. Additionally, we performed targeted patch-clamp analysis of neocortical fast-spiking tdTomato + interneurons to functional assess inhibitory transmission within pharmacologically isolated local GABAergic networks.

Using this multifaceted approach, we show for the first time that GABAergic interneurons undergo DAI, preferentially involving PV+ interneuron PSAI. Additionally, we report a concurrent reduction of inhibitory transmission within local neocortical PV+ interneuron networks. Together, these findings have major implications in neocortical network dysfunction following mTBI.

Materials and Methods

Animals

The Virginia Commonwealth University Institutional Animal Care and Use Committee approved all protocols involving animal maintenance and experimentation. Homozygous PV-Cre (B6;129P2-*Pvalb*$^{tm1(cre)Arbr}$/J; Stock No. 008 069, Hippenmeyer et al. 2005) and reporter line Ai9 (B6.Cg-*Gt(ROSA)26Sor*$^{tm9(CAG\text{-}tdTomato)Hze}$/J; Stock No. 007 909, Madisen et al. 2010) breeding pairs were directly received from Jackson Laboratory. We generated experimental animals (PV-Cre;Ai9 mice) by crossing homozygous male PV-Cre mice with female Ai9 tdTomato reporter mice. In the F1 progeny hemizygous at both alleles, Cre-driven recombination occurs in greater than 90% of *Pvalb*-expressing neurons (Taniguchi et al. 2011). This resulted in selective tdTomato labeling of neocortical PV+ interneurons.

Experimental Design

A total of 38 male PV-Cre;Ai9 mice were randomly assigned to either sham-injury (control) or mTBI experimental groups. For confocal and electron microscopy (EM) studies, a total of 20 mice (8.7–10.9 weeks; 21.1–29.8 g) were surgically prepared for either sham-injury ($N = 5$) or mTBI ($N = 15$) induction. Three mTBI mice were excluded for not meeting previously established criteria (Greer et al. 2011). Based on our previous work, we assessed DAI and downstream structural–functional changes at 3 and 24 h post-mTBI, respectively (Greer et al. 2011; Hånell et al. 2015b). At 3 h post-mTBI, we probed for DAI in PV-Cre;Ai9 mice by analyzing tdTomato+ axonal profiles via parallel confocal microscopy ($n = 5$) and EM ($n = 3$). To further confirm DAI, we compared tdTomato+ axonal profiles against endogenous PV protein and APP immunoreactivity. In a complementary confocal analysis, we tested whether the GABA vesicular transporter (VGAT) and synthesizing enzyme (GAD67) also delineate DAI. As previously reported, between 3 h and 24 h post-mTBI in mice, the distal disconnected axonal segment undergoes Wallerian degeneration, increasing axonal debris. In contrast, by 24 h post-mTBI proximal axonal swelling contiguous with soma of origin begins to resorb, decreasing APP immunoreactivity (Hånell et al. 2015b). Therefore, to comprehensively study the anterograde and retrograde sequelae of tdTomato+ DAI we temporally assessed the relation of the observed axonal debris to nuclear responses in their sustaining somas. Specifically, to identify tdTomato+ somas sustaining DAI while evaluating their fate, we used a previously developed strategy based on retrograde activation of c-Jun via phosphorylation (p-c-Jun), a nuclear transcription factor associated with cell survival and axonal regeneration (Raivich et al. 2004; Greer et al. 2011; Wang et al. 2013). We also employed p-c-Jun as a parallel somatic DAI marker to estimate overall burden of injury in PV-Cre;Ai9 mice at 24 h post-mTBI ($n = 4$). For all qualitative and quantitative confocal assessments sham mice (3 h: $n = 2$; 24 h: $n = 3$) did not reveal any significant differences ($0.5 < P \leq 1.0$; Wilcoxon test). Therefore, 3 and 24 h sham mice were considered as a single control group ($n = 5$) for quantitative analyses of temporal changes following mTBI. Lastly, to probe for any functional correlates of our structural findings, we recorded in slice preparations electrophysiological data from a total of 18 PV-Cre;Ai9 mice (6.0–8.4 weeks; 20.0–26.8 g) at 24 h following sham-injury ($N = 8$) of mTBI ($N = 10$).

Surgical Preparation for Central Fluid Percussion Injury

To model mTBI, we used midline central fluid percussion injury (cFPI) first described by Dixon et al. (1987) using rats, which our laboratory modified for mice as described previously (Greer et al. 2011). Briefly, anesthetized mice were surgically prepared for cFPI induction by installing a hub surrounding a craniectomy centered on the superior sagittal suture, midway between bregma and lambda. Intraoperative rectal temperature was maintained at 37 ± 0.2 °C using a thermostatically controlled heating pad (Harvard Apparatus). Additionally, heart rate (b.p.m.), respiratory rate (r.p.m.), and arterial blood oxygenation (SpO_2) were monitored using a thigh-clamp pulse oximeter sensor (MouseOx; STARR Life Sciences) to ensure maintenance of physiological homeostasis. After a postoperative recovery (~1.5 h), mice were re-anesthetized and then connected to the fluid percussion apparatus (Custom Design & Fabrication, Virginia Commonwealth University) forming a closed mechanical system. Releasing the pendulum, striking the piston in the fluid percussion apparatus generated a mild pressure wave transient (~20 ms) that was delivered onto the intact dura. This action simulates human brain inertial loading during trauma-induced rapid acceleration–deceleration causing diffuse brain injury. The pressure wave (mean peak = 1.6 ± 0.02 SEM atmospheres) was measured by a transducer and displayed on an oscilloscope (Tektronix TDS 210). For sham-injury, an identical procedure was used with the exception of the pendulum's release. Mice were disconnected from the apparatus immediately after injury and visually monitored while removing the hub, suturing the incision, and checking reflexes. None of the mice showed signs of seizure or apnea. Severity of injury and duration of loss of righting reflex (LORR), a rodent behavioral surrogate of loss of consciousness (LOC), were recorded for each animal (Grimm et al. 2015). We determined the degree of mTBI by comparing LORR duration with shams (Morehead et al. 1994). After recovering from LORR, animals were transferred to a warmed cage to maintain normothermia and monitored before returned to the vivarium.

Perfusion and Tissue Processing

Mice received a lethal dose of sodium pentobarbital (1.6 mg/g IP) following 3 or 24 h survival. After loss of pain reflexes mice were transcardially perfused, first with heparinized (10 units/mL) saline for 1 min then 4% paraformaldehyde in Millonig's buffer pH 7.4 for 10–20 min. Brains were dissected and immersed in the same fixative overnight at 4 °C. Mice for EM studies were perfused with 4% paraformaldehyde in Millonig's buffer pH 7.4 supplemented with 0.2% glutaraldehyde. Brains were then section coronally at 40 μm using a vibratome (Leica VT1000S). Sections directly below the craniectomy (bregma level −0.58 to −2.5 mm) were collected in 24-well plates filled with Millonig's buffer pH 7.4. Each well had 2 sections, one rostral from the first series of 24 sections collected and one caudal from the second series of 24 sections (i.e., sections 25–48). Serial sections within a single column were spaced 240 μm apart. For all quantitative studies, we randomly sampled from caudal sections (1.5–2.5 posterior to bregma) due to the consistency with which our mTBI model

generates DAI within a well-defined region of neocortical GM containing S1 (Greer et al. 2011).

Immunohistochemistry

Free-floating sections were rinsed with PBS. Heat-induced epitope retrieval was performed by incubating sections in 10 mM sodium citrate buffer pH 8.5 for 10 min in an 80 °C water bath (Jiao et al. 1999). After cooling to room temperature sections were rinsed with PBS then incubated for 1 h at room temperature with 10% normal goat serum, 2% fish skin gelatin, and 0.5% Triton X-100 in PBS. To mask any potential endogenous mouse immunoglobulin, the blocking buffer was supplemented with Mouse-on-Mouse reagent (MOM; Vector Laboratories, MKB-2213). Then, sections were rinsed with 1% normal goat serum, 1% fish skin gelatin, and 0.5% Triton X-100 in PBS (working buffer). Primary antibody solutions were prepared by diluting with working buffer and the sections were incubated overnight at 4 °C. Specifically, we used antibodies against PV (mouse IgG1, 1:2000, PV235; rabbit, 1:2000, PV27; Swant), RFP (mouse IgG2a, clone 8E5.G7, 1:1000, 200-301-379; rabbit, 1:1000, 600-401-379; Rockland), APP (rabbit, 1:500, Invitrogen, 51–2700; mouse IgG1, clone 22C11, 1:500, Millipore, MAB348), VGAT (polyclonal rabbit, 1:1000; Synaptic Systems, 131 013), GAD67 (mouse IgG2a, clone 1G10.2, 1:1000; Millipore, MAB5406), and p-Ser63 of c-Jun (rabbit, 1:100; Cell Signaling Technology). The following day, sections were rinsed with working buffer and incubated with appropriate goat-derived secondary antibodies conjugated to Alexa Fluor 488, 568, or 633 (1:500: ThermoFisher Scientific) for 2 h at room temperature. After final rinses using working buffer then PBS, sections were mounted on glass slides and cover-slipped using non-hardening Vectashield ± DAPI (Vector Laboratories, H-1000 or H-1200). Note, when labeling p-c-Jun PBS was replaced with TBS.

Mouse immunoglobulin isotype-specific secondary antibodies were used in all studies to optimize the signal-to-noise ratio (Manning et al. 2012). Parallel control studies were conducted to ensure both primary and secondary antibody fidelity (Lorincz and Nusser 2008). In all cases, primary antibody omission abolished immunoreactivity. Secondary antibody specificity evaluated via cross-reactivity showed no signal between all possible primary × secondary host and/or isotype combinations. Also, tdTomato signal photostabilization was achieved using primary RFP antibodies reacted with secondary antibodies conjugated to Alexa Fluor 568.

Confocal Microscopy

Image acquisition was performed using a laser-scanning confocal microscope (LSM 710, Carl Zeiss). Adhering to stereological principles including random sampling, in all quantitative studies the investigator was blinded from the experimental/dependent variable channel while choosing the region-of-interest visualized under epifluorescence. Using a 10× objective (low-magnification) the field-of-view (FOV) was centered over the primary somatosensory cortex (S1) along the dorsolateral edge of the hippocampus. For equal representation of each neocortical layers 2–6, we used continuous laser scanning to guide rotation of the FOV until it was orthogonal to the underlying SCWM. Images were acquired with optimal Nyquist sampling using Plan-Apochromat 10×/0.45 NA (*XY* = 0.41 µm/pixel; *Z* = 5.8 µm), 20×/0.8 NA (*XY* = 0.152 µm/pixel; *Z* = 0.94 µm), and 40×/1.3 NA (*XY* = 0.094 µm/pixel; *Z* = 0.47 µm) oil immersion object lenses. All multichannel images were acquired using sequential scanning at the lowest possible last power to avoid crosstalk (488 Argon, 561 DPSS, and 633 HeNe). Gain and offset were adjusted for optimal signal range. The pinhole was set to 1.0 ± 0.3 Airy units to maintain identical optical slice thickness in multichannel images. Images for quantitative analysis were acquired using identical settings across samples. For qualitative DAI analyses, *z*-stack images captured the entire dimensions of perisomatic/proximal axonal swellings contiguous with the soma of origin, and also the distal disconnected axonal segment up to the initial branch point when possible.

Electron Microscopy

Ultrastructural analysis of tdTomato+ DAI at 3 h post-mTBI was conducted as described previously by our laboratory (Greer et al. 2011; Hånell et al. 2015b). To confirm the fidelity of tdTomato labeling PSAI, we performed photoconversion to follow the same fluorescently labeled profile from confocal imaging to an electron dense reaction product with EM. First, sections were wet-mounted for confocal imaging and then refloated in PBS for EM processing. To immunolabel tdTomato in sections for EM, we employed the same monoclonal RFP antibody (1:1000) used for photostabilization as described above. We converted the fluorescent signal into an electron dense product via routine peroxidase-based immunoreaction visualized using 3,3-diaminobenzidine. Regions containing confocal-identified tdTomato+ PSAI profiles were located in plastic embedded tissue sections using standard light microscopy. These regions were removed and used for sectioning. One thick section (0.5–1 µm) was cut before collecting thin serial sections (70 nm) and saved to guide location of the labeled neuron of interest. Ultrastructural analysis was performed using a JEM-1230 transmission electron microscope (JEOL-USA) equipped with an Ultrascan 4000SP and Orius SC1000 CCD cameras (Gatan).

Quantitative Confocal Image Analysis

An investigator blinded to experimental/dependent variables performed all quantitative image analyses. Confocal images were imported into Fiji (ImageJ) then processed and analyzed using custom written macros. For automated analyses, objects were segmented from background subtracted 8-bit images by converting into binary using a minimum gray-value threshold. Varying the threshold ±10 gray-values did not change the overall pattern of results. For colocalization studies, we isolated spatially overlapping objects (Ch1+/Ch2+) using the "Image Calculator" function. The "Particle Analysis" function with appropriate size and shape exclusion filters was used to determine the total number of objects per unit area (FOV). To determine the appropriate statistical unit for continuous data, we analyzed the means of the differences between images of ipsi- and contra-lateral hemispheres within each individual group, and also across different experimental groups. There were no statistically significant differences (*P*-values ranging from 0.1 to 1.0; Wilcoxon Signed Rank test); therefore, we considered the statistical unit as a single section. To determine the total count per section, we summed the number of objects (particles) per FOV of ipsi- and contra-lateral hemispheres. We divided the sum of particles per section by the combined area to yield a normalized density reported as particles/mm^2.

We used pixel-based intensity correlation to assess the overlap of tdTomato expression with PV and RFP immunoreactivity specifically in axons and dendrites. A minimum and

maximum threshold were applied to subtract background and exclude the high-intensity signals from neuronal somas, respectively. The "Colocalization Finder" function was used to measure pixel intensity spatial correlation, which yields a Pearson's Correlation Coefficient (Rr). The percentage of soma overlap and the Pearson's Rr were then averaged for each group (tdTomato/PV: $n = 6$ FOV from 3 mice; tdTomato/RFP: $n = 4$ FOV from 2 mice).

GABAergic Markers of DAI

Currently, there are no neuronal class-specific DAI markers. To establish a GABAergic-specific DAI marker, we performed a 2-part (visual and automated) quantitative colocalization analysis. From each animal ($n = 5$) 4 serial sections starting at a random well (#1–6) were double labeled for GAD67 and APP. The first section from each series was saved for a pilot study described below and the remaining sections were used for quantitative colocalization analyses. Low-magnification (10× objective) full-section z-stacks captured GAD67 and APP immunoreactive profiles in S1 layers 2–6. Visual analysis of low-magnification images yielded 97% accuracy of identifying GAD67+/APP+ axonal swellings ($N = 183$) from GAD67+ profiles ($N = 189$). To quantitatively assess colocalization with native tdTomato expression single optical slices through the center of each GAD67+/APP+ axonal swelling were acquired using a 20× objective at 3× zoom. We estimated the percentage of neocortical GABAergic DAI represented by PV+ interneurons from the frequency of GAD67+/APP+ axonal swellings that were tdTomato+ ($N = 158$) and tdTomato– ($N = 25$) and compared the proportions that occurred in the perisomatic domain.

Further, we performed quantitative colocalization analysis to determine if GAD67+ accumulations (particles) are a positive predictor of APP+ axonal swellings at 3 h post-mTBI. Automated object-based colocalization analysis of maximum intensity projections segregated the population of GAD67+ particles that were and were not colocalized with APP. We determined the optimal threshold area of axonal swellings by analyzing GAD67+ particle size distribution varying as a function of APP colocalization in the first serial section from each animal. From these subpopulations, we determined maximum (30 μm^2) and minimum (5 μm^2) threshold areas to minimize quantification of individual and/or clusters of GAD67+ presynaptic boutons, respectively. We found that a GAD67+ particle size threshold of 10 μm^2 predicted APP colocalization with a 76% sensitivity and 96% specificity. Using the remaining serial sections, we determined the frequency of GAD67+ particles with areas above ($N = 138$) and below ($N = 799$) the 10 μm^2 threshold and compared the proportions that colocalized with APP+ axonal swellings.

p-c-Jun Expression Following tdTomato+ Interneurons PSAI

Continuous tdTomato+ PSAI profiles traceable back to the soma of origin provided a unique opportunity to follow retrograde changes. We evaluated p-c-Jun expression at 3 h post-mTBI, when tdTomato+ PSAI was readily identified. Randomly selected single sections per animal ($n = 5$) were labeled for p-c-Jun. To attain a sufficient sample size while retaining adequate resolution we used a 20× objective to acquire full-section z-stacks. The FOV was centered in S1 layer 5, which has highest density of PV+ interneurons (Rudy et al. 2011; Pfeffer et al. 2013). All tdTomato+ interneurons were counted to ensure the samples were representative. First, an investigator blinded to the p-c-Jun channel visually identified and marked tdTomato+ somas with PSAI morphological profiles within a 20 μm radius ($N = 22$). The remaining unmarked tdTomato+ interneurons were considered non-PSAI/intact ($N = 497$). Object-based colocalization analysis isolated tdTomato+/p-c-Jun+ somas and the proportions overlapping with marked (PSAI morphology) and unmarked (non-PSAI/Intact) profiles were compared.

Anterograde and Retrograde Sequelae of tdTomato+ Interneuron PSAI

Previously, we showed anterograde changes following PSAI involve rapid axonal disconnection and Wallerian degeneration (Kelley et al. 2006), which is associated with widespread terminal loss (Erb and Povlishock 1991; Povlishock et al. 1992). Also, we reported that the retrograde consequences of DAI do not involve cell death (Singleton et al. 2002). Rather, DAI neurons express p-c-Jun (Greer et al. 2011; Wang et al. 2013), a nuclear transcription factor associated with cell survival and axonal regeneration (Raivich et al. 2004). Here, we quantitatively analyzed the densities of tdTomato+ axonal debris and tdTomato+/p-c-Jun+ interneurons in mice following sham-injury ($n = 5$), 3 h mTBI ($n = 5$), and 24 h mTBI ($n = 4$). Based on mean ± standard deviation (SD) of pilot data, we determined one randomly selected section per animal would be sufficient to detect a significant difference in tdTomato+/p-c-Jun+ density between sham and 24 h post-mTBI. During immunohistochemical processing, one of the 3 h mTBI sections was lost to damage. Automated object-based analysis was used to quantify the density of axonal debris, tdTomato+/p-c-Jun+ interneurons, and total tdTomato+ and p-c-Jun+ populations. The numbers of tdTomato+/p-c-Jun+ somas were used to estimate overall burden of injury with respect to the total tdTomato+ interneuron population and pan-neuronal DAI (pyramidal and interneuron) p-c-Jun+ nuclei population.

Electrophysiology

To determine functional correlates of tdTomato+ interneuron PSAI, we probed for disruption of GABAergic transmission in local neocortical inhibitory networks. In a separate cohort of mice, acute slice preparation, patch-clamp recordings, and data analysis were performed as described in our previous reports (Hånell et al. 2015a; Sun and Jacobs 2016). Briefly, we recorded spontaneous inhibitory postsynaptic currents (sIPSCs) in tdTomato+ interneurons within layer 5 of S1BF in ex vivo coronal slices 24 h after sham-injury ($N = 8$) or mTBI ($N = 10$). To isolate sIPSC from excitatory currents, the normal artificial cerebral spinal fluid bathing medium was supplemented with glutamate receptor antagonists (50 mM APV and 20 mM DNQX). The intracellular solution (E_{Cl}– = –15 mV) contained (in mM): 70 K-gluconate, 70 KCl, 10 Hepes, 4 EGTA, 4 Na-ATP, and 0.2 Na-GTP, and 0.05–0.2% biocytin conjugated to Alexa Fluor 488 (ThermoFisher Scientific). IPSCs were recorded from tdTomato+ interneurons held 3 min under voltage-clamp at –60 mV and data having more than 200 events were analyzed. Action potentials were recorded using current-clamp of tdTomato+ interneurons maintained at –60 mV and analyzed from individual sweeps with 8 or more events. For post hoc morphological analysis sections were immersed in 4% paraformaldehyde pH 7.4 in PBS for 2 h at room temperature and then stored in PBS. Immunohistochemistry for p-c-Jun was performed as described above. Biocytin was reacted with streptavidin conjugated to Alexa 488 (1:1000; ThermoFischer Scientific) during the secondary antibody incubation step. Electrophysiological recordings were acquired from a total of 46 tdTomato+

fast-spiking PV+ interneurons (Sham n = 18; mTBI n = 28). Individual neurons were considered as the statistical unit.

Statistics

Data analysis was performed using JMP Pro version 12.2.0 (SAS Institute) software. Continuous data sets were assessed for normality using quantile (QQ) plots and the Shapiro–Wilk test. Normal data are summarized using mean ± SD with corresponding 95% confidence intervals (CI). Significant differences in normally distributed data were determined using parametric tests. In all analyses, the variance was not significantly different between groups ($P > 0.05$, Brown–Forsythe test). Statistically significant differences were determined between 2 groups that were either independent or dependent using unpaired and paired t-test, respectively. For multiple groups, we performed one-way ANOVA followed by post hoc comparisons of all pairs using the Tukey–Kramer HSD test. Continuous data distributions deviating from normality were summarized using medians with interquartile range (IQR), and analyzed with nonparametric statistical tests. Statistically significant differences between 2 groups were determined using the Wilcoxon test. Multiple groups were statistically analyzed using the Kruskal–Wallis test followed by post hoc comparisons with control (sham-injury group) using the Dunn method for joint ranking. The Pearson and Spearman tests were used to determine significant correlations between parametric and nonparametric data sets, respectively. For categorical data the proportions of dichotomous groups were compared using 2 × 2 contingency analysis. Significant differences were determine using a X^2 (chi-squared) test if the expected frequencies were greater than 5; otherwise, the group proportions were analyzed with the Fisher's exact test. All statistical tests were 2-tailed and the significance threshold was $\alpha = 0.05$.

Results

Intraoperative Physiology and Mild cFPI

Intraoperative physiology was normal and consistent with previous reports on mice under isoflurane anesthesia (Cesarovic et al. 2010; Ewald et al. 2011; Hånell et al. 2015b). For mice used in morphological studies, mean ± SD arterial oxygen saturation (sham = 97.6 ± 0.2%; 3 h mTBI = 97.7 ± 0.5%; 24 h mTBI = 98.1 ± 0.4%), heart rate (sham = 553 ± 23 b.p.m.; 3 h mTBI = 565 ± 17 b.p.m.; 24 h mTBI = 536 ± 55 b.p.m.), and respiratory rate (sham = 67 ± 9 r.p.m.; 3 h mTBI = 62 ± 9 r.p.m.; 24 h mTBI = 66 ± 6 r.p.m.) were similar across all groups (arterial oxygen saturation: $F_{2,13} = 2.80$, $P = 0.1005$; heart rate: $F_{2,13} = 0.81$, $P = 0.4688$; respiratory rate: $F_{2,13} = 0.58$, $P = 0.5758$; one-way ANOVA). Also, in the mice used for electrophysiological analysis, arterial oxygen saturation (sham = 97.5 ± 0.7%; mTBI = 97.8 ± 0.3%), heart rate (sham = 555 ± 36 b.p.m.; 24 h mTBI = 524 ± 44 b.p.m.), and respiratory rate (sham = 68 ± 5 b.p.m.; 24 h mTBI = 68 ± 6 b.p.m.) were similar between groups (arterial oxygen saturation: $t_{16} = 1.15$, $P = 0.2785$; heart rate: $t_{16} = -1.25$, $P = 0.2380$; respiratory rate: $t_{16} = 0.01$, $P = 0.9896$; unpaired t-test). Importantly, signs of hypoxia were not observed (minimal respiratory rate 50 ± 17 r.p.m., 95% CI: 54–69 r.p.m.) and ≥95% oxygen saturation was maintained throughout the duration of the surgery. Overall, these physiological assessments did not show any evidence of confounding mechanisms that play a role in secondary insults.

The LORR duration was significantly greater in mTBI mice compared with shams and consistent with our previous reports (Greer et al. 2011, 2013; Hånell et al. 2015b). For mice used in morphological studies, there was a significant difference in LORR duration between sham and mTBI groups ($F_{2,13} = 40.66$, $P < 0.0001$; one-way ANOVA). Specifically, post hoc comparisons showed LORR duration of both 3 h mTBI (4.8 ± 0.8 min, 95% CI: 3.9–5.7 min) and 24 h mTBI (4.3 ± 0.9 min, 95% CI: 3.2–5.4 min) groups to be significantly longer ($P < 0.0001$; Tukey–Kramer HSD) compared with shams (1.1 ± 0.3 min, 95% CI: 0.7–1.4 min). No significant difference in LORR duration was observed between the 3 h and 24 h mTBI groups ($P = 0.4317$). Similarly, in mice used for electrophysiological analysis there was a significant difference in LORR duration between sham (1.2 ± 0.7 min, 95% CI: 0.3–2.1 min) and mTBI (5.0 ± 2.0 min, 95% CI: 3.6–6.4 min) groups ($t_{16} = 4.01$, $P = 0.0015$; unpaired t-test). No significant differences in LORR duration were observed between morphological and electrophysiological groups (sham: $t_{11} = -0.47$, $P = 0.6479$; mTBI: $t_{23} = -0.63$, $P = 0.5383$; unpaired t-test). Lastly, no animals were lost to anesthesia, surgical preparation, or mild cFPI.

Macroscopically, both sham and mTBI brain tissues appeared normal without evidence of surgically induced lesions as previously reported (Kelley et al. 2006; Greer et al. 2011; Hånell et al. 2015b). Post-mTBI tissue sections revealed little to no macroscopic change consistent with the mild and diffuse nature of cFPI (Dixon et al. 1987; Johnson et al. 2015; Lifshitz et al. 2016). Importantly, the dorsal neocortex underneath the craniectomy site did not show evidence of focal contusion, cavitation, or overt subarachnoid hemorrhage induced by the fluid pressure wave. Overall, the brain parenchyma was devoid of overt hemorrhage, with only isolated petechial hemorrhage observed in the corpus callosum of 8/21 mTBI mice. At all survival times, the ventricular system maintained a regular contour, with no evidence of trauma-related ventricular enlargement. Taken together these data support our premise that cFPI in PV-Cre; Ai9 mice is a reproducible model of mTBI.

Characterization of PV-Cre;Ai9 Mice and tdTomato Photostabilization

PV-Cre;Ai9 mice provided a homogenous and reliable system to probe for PV+ interneuron DAI. To enable optimal analysis of PV+ interneuron fine axonal structure, we fluorescently labeled cells by crossing PV-Cre mice with the Ai9 Cre-dependent tdTomato reporter line. PV+ interneurons were selectively labeled with tdTomato across neocortical layers 2–6, where broad colocalization with endogenous PV protein immunoreactivity was observed (Fig. 1A). Expression specificity between the Cre-dependent tdTomato reporter and the endogenous *Pvalb* gene was quantitatively assessed via immunofluorescence using a monoclonal antibody against PV protein (Fig. 1B–D,J). A high degree of expression specificity was observed using both object-based analysis of soma overlap (mean, 95% CI: 93, 89–96% of tdTomato expressing somas were PV+; and 95, 93–97% of PV+ somas expressed tdTomato) and pixel intensity spatial correlation of dendrites and axons (Pearson's $Rr = 0.81$). To stabilize the tdTomato fluorescent signal and increase the visibility of slender axonal fibers (Fig. 1H), we used an additional approach that employed primary antibodies against RFP that recognize tdTomato (Fig. 1E–G). Specificity of RFP antibodies used throughout this study was tested via immunoreaction with sections from PV-Cre;Ai9 (positive control; Fig. 1E–G) and wild-type C57BL/6 (negative control; Fig. 1I) mice, the background strain for both the PV-Cre and Ai9 knock-in gene targeted mice (Hippenmeyer et al. 2005; Madisen et al. 2010). In the PV-Cre;Ai9 positive control (Fig. 1E,F), immunoreaction with RFP antibodies was visualized using secondary antibodies

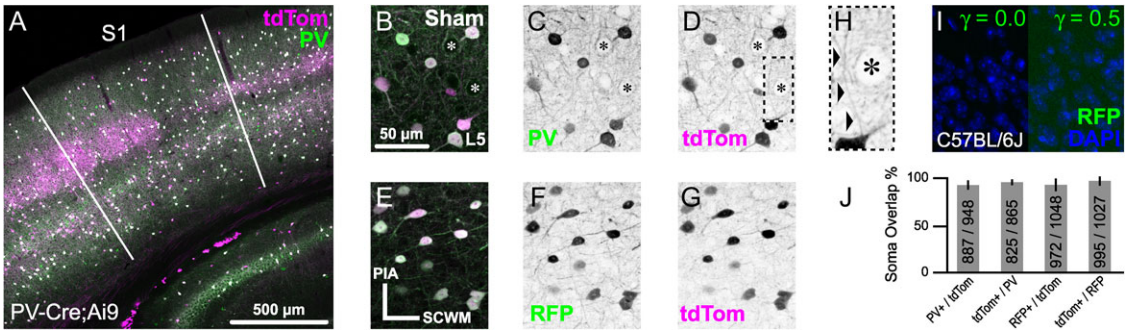

Figure 1. Characterization of PV-Cre;Ai9 mouse and RFP antibody for enhanced visualization of tdTomato expression. *A–H*, Representative maximal intensity projections from sham-injured PV-Cre;Ai9 mice that express tdTomato (tdTom) in PV+ interneurons. All images are oriented perpendicular to the SCWM (*E*). (*A*) Overview image of a coronal section showing broad overlap between native tdTomato expression and endogenous PV immunoreactivity with S1 delineated. *B–G*, Higher-magnification images showing colocalization of tdTomato with PV (*B–D*) and immunoreaction using antibodies against RFP (that recognize tdTomato; *E–G*) within layer 5 neocortex. (*B–D*, *H*) Typical profiles of tdTomato+/PV+ perisomatic innervation of a layer 5 pyramidal neuron (asterisks). (*H*) Zoomed image of box in *D*, showing an ascending axonal projection (arrowheads) juxtaposed by tdTomato+ presynaptic terminals with characteristic "basket" morphology. Note the fine diameter of the axon (~0.5 µm), which could be followed for ~30 µm distal to the soma of origin. *E–G*, Colocalization of tdTomato with RFP immunoreactivity, which was visualized using secondary antibodies conjugated to Alexa Fluor 488 (*F*). Parallel anti-RFP immunoreaction in a C57BL/6 J (WT) tissue section (*I*), the background strain of PV-Cre and Ai9 mice, did not reveal evidence of non-specific binding. (*J*) Summary data (mean with 95% CI error bars and cell counts) from quantitative colocalization analysis of expression specificity between Cre-driven tdTomato and endogenous PV (n = 6 FOV from 3 animals) and native tdTomato signal with RFP immunoreactivity (n = 4 FOV from 2 animals) within neocortical layers 2–6.

conjugated to Alexa Fluor 488 (Fig. 1*F*), revealing broad colocalization with tdTomato expression (Fig. 1*E–G*). Similar to PV immunoreactivity (Fig. 1*J*), a high degree of RFP antibody specificity was observed using both object-based analysis of soma overlap (mean, 95% CI: 93, 87–98% of tdTomato expressing cells were RFP+; and 97, 93–100% of RFP immunoreactive cells were tdTomato+) and pixel intensity spatial correlation (Pearson's Rr = 0.83). However, in the parallel negative control reaction, no RFP immunoreactivity was observed in wild-type C57BL/6 sections (Fig. 1*I*). The robust and reliable expression of tdTomato as well as its intrinsic brightness, coupled with its photostabilization, allowed for detailed, high fidelity analysis of the fine axonal structure of PV+ interneurons.

Evidence for PV+ Interneuron DAI Demonstrated by tdTomato Expression

PV-Cre;Ai9 mice following sham or mTBI showed major differences in their tdTomato+ profiles. No tdTomato+ profiles indicative of DAI were observed in shams (Fig. 1*D,G*). Axons arising from tdTomato+ somas were fine caliber (~0.5 µm). With respect to the soma of origin, tdTomato+ axons could be traced approximately 30 µm distally to their initial branch point where secondary fibers then became difficult to follow (Fig. 1*H*). Following mTBI, despite the macroscopic preservation of brain parenchymal integrity, cFPI consistently evoked microscopic tdTomato+ axonal pathology revealing DAI throughout the dorsolateral neocortex (Fig. 2). At 3 h post-mTBI PV-Cre;Ai9 mice showed readily identified tdTomato+ axonal swellings (~5 µm in diameter) proximal to their soma of origin (within 20 µm) scattered across S1 layers 2–6 (Fig. 2*A–F*). Most of these tdTomato+ axonal swellings were in continuity with their soma of origin, consistent with PSAI described in our previous communications (Singleton et al. 2002; Kelley et al. 2006; Greer et al. 2013; Hånell et al. 2015b). Axonal segments between perisomatic swellings and their somas retained a normal caliber (Fig. 2*F*). The majority of tdTomato+ PSAI coursed toward the cortical pial surface (Fig. 2*A–F*), consistent with PV+ interneuron morphological characteristics (Markram et al. 2004). Less frequently, smaller isolated tdTomato+ globular profiles were found, suggesting potential sites of axonal injury remote from their soma of origin. The tdTomato+ distal axonal segments disconnected from their perisomatic/proximal axons revealed anterograde change reflected in bulbous, multilobular varicosities (Fig. 2*F*). Typically, these disconnected distal axonal segments could be traced to their initial branch point, indicating that tdTomato+ PSAI leads to disconnection and degeneration of the entire distal axonal arbor (Fig. 2*H*). At 24 h post-mTBI (Fig. 2*H–K*) the tdTomato+ PSAI profiles were difficult to identify. In contrast, readily observable were dense tdTomato+ globules ranging from 1 to 5 µm in diameter scattered throughout regions of neocortical DAI, again consistent with progressive anterograde degeneration of disconnected distal axonal segments (Fig. 2*I,J*) and their associated terminals (Fig. 2*K*).

The parallel use of RFP antibodies not only helped stabilize and enhance the tdTomato signal, but also allowed the confirmation of these confocal microscopy findings (Fig. 2*A–G*; Fig. 3*A,B*) with ultrastructural analysis (Fig. 3*C–E*). Photoconverting the fluorescent signal into an electron dense reaction product via routine peroxidase-based methods allowed visualization of the same tdTomato+ interneuron using both confocal (Fig. 3*A,B*) and EM (Fig. 3*C–E*). At 3 h post-mTBI, ultrastructural analysis of a tdTomato+ PSAI interneuron revealed a proximal axonal swelling, contiguous with its soma, that was laden with organelles and vesicles (Fig. 3*E*), pathognomonic of focal impaired axonal transport (Povlishock 1993). The associated disconnected distal segment showed evidence of cytoskeletal disorganization and the rapid onset of Wallerian degeneration (Fig. 3*D*).

APP Expression after mTBI: Linkage to tdTomato+/PV+ Interneuron Axonal Changes

Neocortical tdTomato+/PV+ interneuron DAI was also confirmed using APP immunofluorescence. The focal intra-axonal vesicle accumulations seen in EM images (Fig. 3*E*) were detected indirectly using confocal microscopy by targeting APP (Fig. 4*B,F,J*). At 3 h post-mTBI, APP+ axonal swellings were observed across S1 layers 2–6 as well as the underlying SCWM (Fig. 5*A*). To confirm neocortical PV+ interneuron DAI, we labeled APP to determine the extent of colocalization at sites of

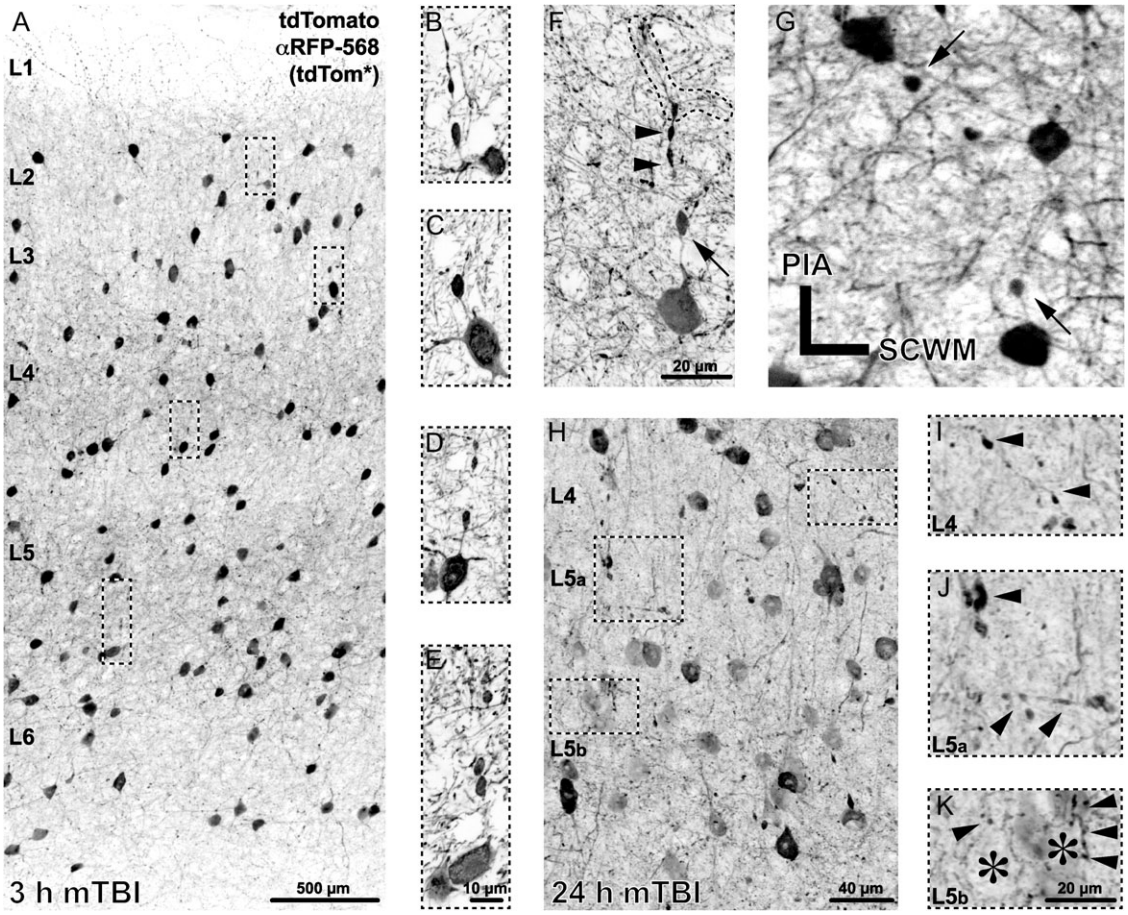

Figure 2. Repertoire of tdTomato+ neuropathology following mTBI. Representative images of tdTomato+ morphological changes at 3 h (*A–G*) and 24 h (*H–K*) post-mTBI. (*A–E*) Within 3 h post-mTBI, tdTomato+ axonal swellings, occurring near the soma of origin, were observed across S1 layers 2–6. (*F*) A representative tdTomato+ interneuron showing a perisomatic axonal swelling (arrow, oriented toward pia) and the distal disconnected axonal segment with lobular/varicose morphology (arrowheads) that can be traced to the initial branch point (outline). While the majority of tdTomato+ perisomatic axonal swellings were oriented toward the pia (*A–F*), occasionally profiles with descending and/or lateral trajectories were found (*G*). (*H–K*) At 24 h post-mTBI, perisomatic axonal swellings were difficult to identify; however, widespread tdTomato+ axonal debris was readily observable. (*I–K*) Zoomed images corresponding to insets in *H*, reflecting progressive tdTomato+ anterograde changes (arrowheads) likely associated with distal disconnected axonal arbor (*F*) degeneration. (*K*) Layer 5 pyramidal neuron silhouettes (asterisks) showing evidence of tdTomato+ axonal terminal degeneration, ranging from punctate (left arrowhead) to varicose (right arrowheads) profiles.

tdTomato+ PSAI and endogenous PV protein to verify the identity of tdTomato+ interneurons. At 3 h post-mTBI, we observed elevated tdTomato expression and PV immunoreactivity within APP+ perisomatic axonal swellings (Fig. 4*A–D*). APP immunoreactivity was restricted to the evolving perisomatic/proximal axonal swelling, with the distal surface demarcating the site of disconnection (Fig. 4*B*). In contrast, the disconnected distal axonal segments were always devoid of APP immunoreactivity, consistent with previous findings from our laboratory using transgenic mice (Greer et al. 2011; Wang et al. 2011; Hånell et al. 2015b). Characteristic of DAI, we found these APP+ axonal swellings juxtaposed non-DAI (intact) tdTomato+/PV+ axonal profiles (Fig. 4*A–D*). Similar to observations in shams (Fig. 1*H*), intact tdTomato+ axons could be followed up to approximately 30 μm distal to their soma of origin (Fig. 4*C*) and in the absence of any pathologic morphology there was also no detectable intra-axonal APP immunoreactivity (Fig. 4*B*). Based on our quantitative analysis of tdTomato/PV overlap (Fig. 1*J*) and the demonstration of tdTomato+/PV+ PSAI colocalizing with APP+ swellings (Fig. 4*A–D*) we considered tdTomato and PV proteins as synonymous molecular interneuron markers for subsequent studies described below.

Complementary Approaches Employing GABAergic Markers to Further Validate PV+ interneuron DAI

Based on our finding of APP+ immunoreactivity in tdTomato+ PSAI, we tested whether VGAT and GAD67, vesicle-associated proteins (Kanaani et al. 2010) found in presynaptic boutons (Fish et al. 2011), would also accumulated at sites of impaired axonal transport. Qualitative (Fig. 4) and quantitative (Fig. 5) analyses were conducted at 3 h post-mTBI due to the ease with which PSAI/DAI could be identified via tdTomato expression and APP immunoreactivity. S1 layers 2–6 demonstrating APP+ axonal swellings also revealed VGAT (Fig. 4*E–H*) and GAD67 (Fig. 4*I–L*) immunoreactive profiles that colocalized with tdTomato+ PSAI. These VGAT+ or GAD67+ accumulations were dramatically larger than the surrounding immunoreactive presynaptic boutons (0.5–2.5 μm in diameter) and overlapped with APP+ axonal swellings. Signal intensity of GAD67+ (Fig. 4*C*) accumulations were comparable to tdTomato+ PSAI (Fig. 4*G*) and showed a better signal-to-noise than VGAT immunoreactive swellings (Fig. 4*E*) with respect to surrounding presynaptic boutons.

Low-magnification overview images further demonstrated the utility of targeting GAD67 to not only identify GABAergic

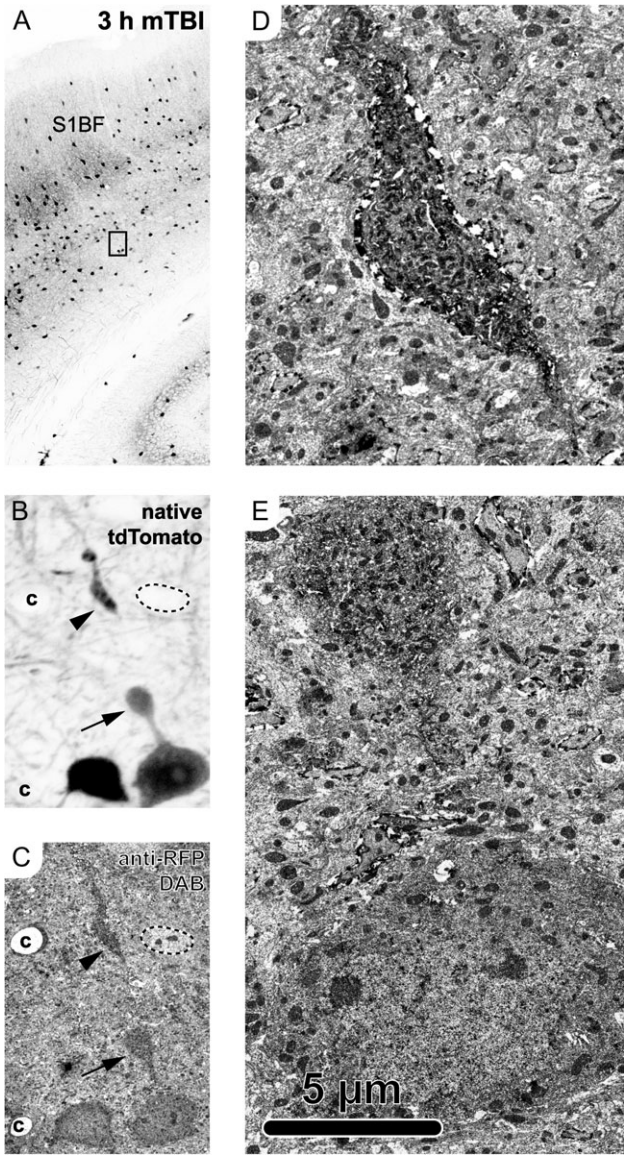

Figure 3. Ultrastructural analysis of tdTomato+ PSAI identified via confocal microscopy. The same tdTomato+ profile was followed from the light (*A*,*B*) to electron (*C–E*) microscopy level at 3 h post-mTBI. (*A*, *B*) Confocal images capturing native tdTomato signal. (*A*) Overview image of S1BF with inset in layer 5/6 corresponding to tdTomato+ neuron in *B*, showing PSAI (arrow, oriented toward pia) and related disconnected distal segment (arrowhead). Employing the same RFP antibodies used for photostabilizing allowed use to follow the same tdTomato+ neuron from confocal (*B*) to electron (*C–E*) microscopy level. (*C*) The tdTomato+ neuron was identified based on morphology, including the perisomatic axonal swelling (arrow) and disconnected distal axonal segment (arrowhead), as well as other fiduciary markers including an adjacent tdTomato+ neuron (left), nearby capillaries (c), and a non-tdTomato expressing neuron adjacent to the tdTomato+ disconnected distal axonal segment (outline, upper right). (*D–E*) Ultrastructural analysis of the tdTomato+ distal disconnected segment (*D*) showed disorganized cytoskeleton consistent with the onset of Wallerian degeneration and the perisomatic swelling (*E*) laden with organelles and vesicles, indicating a focal site of impaired axonal transport.

DAI but also provide a high-throughput and reliable means of quantifying the burden of injury, wherein the nearest neighboring axonal swelling could be several hundred microns away (Fig. 5A). In low-magnification (×10 objective) z-sacks images, 183/189 visually identified GAD67+ profiles colocalized with APP+ axonal swellings verified in higher-magnification (×20 objective) single optical slice images. Visual quantification of GAD67+/APP+ axonal swellings in S1 layers 2–6 (Fig. 5A, arrows) yielded a mean density (swellings/mm^2) of 8.4 (95% CI: 6.4–10.5). The majority of GAD67+/APP+ axonal swellings (mean ± SD) colocalized with tdTomato (88 ± 7%, 95% CI: 84–92.0%), which was significantly greater (t_{14} = 19.83, $P < 0.0001$; paired *t*-test) than the tdTomato– population (12 ± 7%, 95% CI: 8–16%). To confirm the association between GAD67+ axonal swellings with APP immunoreactivity, we quantified the overlap between the spatial distributions with respect to the size of GAD67+ and APP+ axonal swellings via automated object-based analysis (Fig. 5A, outlines). Automated quantitation yielded a density (swellings/mm^2: 8.1, 95% CI: 6.2–10.0) almost identical to the visual approach (t_{14} = 0.67, P = 0.5117; paired *t*-test), and displayed a strong significant correlation (Pearson's r = 0.82, P = 0.0002). Having established a consistent and systematic method of quantifying the total number of axonal swellings, we then compared the size distributions of GAD67+ accumulations (Fig. 5C) and found a statistically significant difference with respect to colocalization with APP+ axonal swellings ($P < 0.0001$). Approximately 82% of GAD67+ profiles with areas greater than 10 µm^2 (~3.5 µm in diameter) colocalized with APP+ axonal swellings, which was nearly 10-fold more than profiles below this size threshold (Fig. 5C). Accordingly, our results show that GAD67 immunoreactivity is a positive predictor of APP+ axonal swellings with sensitivity = 66% (95% Score CI: 57–71%), specificity = 97% (95% Score CI: 95–98%), and odds ratio = 54 (95% CI: 32–89).

PV+ Interneuron DAI Occurs Primarily within the Perisomatic Domain

The majority of tdTomato+ DAI occurred within 30 µm from the soma of origin. Relative to the terminal tdTomato+ axonal swelling, the noninjured proximal axonal segment could be continuously traced back to the soma of origin (Fig. 2*F*). Less frequently, isolated DAI remote from the soma of origin was identified via colocalization of GAD67 and APP immunoreactivity (Fig. 5B, bottom row). To validate our qualitative findings, we performed a complementary quantitative analysis determining whether the same population of visually identified GAD67+/APP+ axonal swellings analyzed above was significantly correlated with tdTomato+ PSAI (Fig. 5B, top row). Corroborating our qualitative observations, GAD67+/APP+/tdTomato+ swellings were significantly associated with the PSAI ($P < 0.0001$), representing approximately 78% of total tdTomato+ DAI (Fig. 5D), and accounting for 98% (123/124) of the total GAD67+/APP+ PSAI population (Fig. 5B, top and middle rows). Qualitative inspection of the ~22% remote swellings demonstrated several tdTomato+ profiles that appeared to be disconnected from their somas of origin, which were either likely outside the optical plane, or a relatively small (about 2–3 µm diameter) subpopulation that was often located in neocortical layer 6, near the SCWM interface. Taken together, these approaches demonstrate that visual detection of PV+ interneuron PSAI via tdTomato+ profiles is reliable, affording us the unique opportunity to assess retrograde consequences.

Anterograde and Retrograde Sequelae of PV+ interneuron PSAI

Our results also confirm that tdTomato+ interneuron PSAI is significantly associated with retrograde p-c-Jun nuclear expression. Importantly, in shams tdTomato+ abnormalities and p-c-Jun immunoreactivity were virtually absent (Fig. 7A). In contrast, within 3 h post-mTBI the occurrence of tdTomato+ PSAI

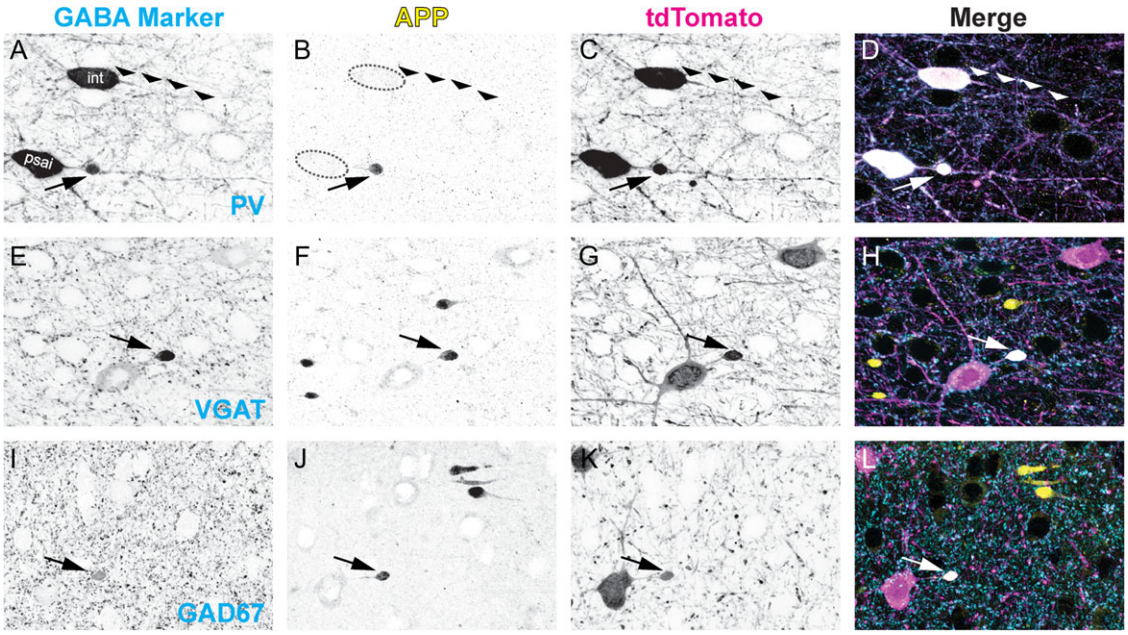

Figure 4. GABAergic markers accumulate in APP+/tdTomato+ perisomatic axonal swellings. Representative images at 3 h post-mTBI showing GABAergic markers (*A*, *E*, *I*) with respect to APP immunoreactivity (*B*, *F*, *J*), which accumulates at focal sites of impaired axonal transport (arrows). Colocalization of tdTomato+ PSAI with PV (*A–D*), VGAT (*E–H*), and GAD67 (*I–L*) immunoreactivity confirms GABAergic interneuron axonal injury. (*A*) Normal uninjured intact (int) axonal profile (wide arrowheads) juxtaposed by PV+ interneuron PSAI (arrow). (*B*) APP is not detected within the intact axonal profile, while robust APP immunoreactivity colocalizes with tdTomato+/PV+ interneuron PSAI (*C*, *D*). Within sites of tdTomato+ PSAI (*C*,*G*,*K*), the immunoreactive profiles of VGAT (*E*) and GAD67 (*I*) are similar to APP+ axonal swellings (*F* and *J*, respectively). Qualitatively, the GAD67+ axonal swelling profile (*I*, *L*) has a better signal-to-noise than VGAT (*E*, *H*). Note non-GABAergic APP+ axonal swellings have opposite trajectories.

coincided with increased p-c-Jun expression throughout S1 layers 2–6 (Fig. 7*B*). These tdTomato+ PSAI profiles could be traced back to the soma of origin (Fig. 6A), providing a unique opportunity to follow retrograde changes. Quantitative analysis of visually identified PSAI profiles showed that 64% of tdTomato+ somas colocalized with nuclear p-c-Jun immunoreactivity, reflecting a significant ($P < 0.0001$) and rapid retrograde response (Fig. 6*A*,*B*). In contrast, only 1.6% of tdTomato+ somas with no apparent PSAI overlapped with p-c-Jun+ profiles. Post hoc inspection of tdTomato PSAI+/p-c-Jun– (false positive; Fig. 6*C*) and tdTomato PSAI–/p-c-Jun+ (false negative; Fig. 6*D*) subsets revealed tdTomato+ profiles that were more likely perisomatic dendritic branch points and subtle PSAI obscured by surrounding neurites, respectively. Accordingly, our results show that nuclear p-c-Jun expression is a retrograde surrogate marker of tdTomato+ PSAI with sensitivity = 64% (95% Score CI: 43–80%), specificity = 98% (95% Score CI: 97–98%), and odds ratio = 107 (95% CI: 35–326). Validating nuclear expression of p-c-Jun as a reliable surrogate tdTomato+ PSAI marker and establishing fluorescent-based methodologies for assessing axonal morphology, allowed use to follow both retrograde and anterograde changes overtime, respectively (Fig. 7).

Retrograde p-c-Jun nuclear expression and anterograde disconnected distal axon degeneration evolved rapidly overtime leading to a substantial tdTomato+ burden of injury (Fig. 7*A–C*). As described above, we showed tdTomato+ interneuron involvement following mTBI by examining nuclear changes in somas connected to PSAI. Consistent with distal axon degeneration following disconnection from perisomatic/proximal axonal swellings, the densities of tdTomato+ debris and tdTomato+/p-c-Jun+ somas, respectively, were significantly correlated (Spearman $\rho = 0.74$, $P < 0.0041$). Temporal analysis showed the densities of tdTomato+ axonal debris ($P = 0.0291$; Fig. 7*D*) and tdTomato +/p-c-Jun+ somas ($P = 0.0053$; Fig. 7*E*) were significant different between sham, 3 h mTBI, and 24 h mTBI groups. Specifically, at 24 h post-mTBI, the densities of tdTomato+ axonal debris and tdTomato+/p-c-Jun+ somas were both significantly different from sham ($P = 0.0381$ and $P = 0.0034$, respectively). Notably, between 3 h and 24 h post-mTBI tdTomato+/p-c-Jun+ density increased 5-fold (Fig. 7*H*). Despite cFPI consistently evoking widespread tdTomato+ axonal pathology that evolved overtime along with increased p-c-Jun expression, overt tissue damage and tdTomato+ interneuron loss ($P = 0.4401$; Fig. 7*G*) were not observed. However, the overall DAI burden (median, IQR) with respect to the total population of tdTomato+ interneurons and p-c-Jun+ nuclei (i.e., total population of neocortical neuron DAI) was substantial. At 24 h post-mTBI we found 8.7, 4.6–13.2% tdTomato+ interneurons expressed p-c-Jun (Fig. 7*H*), representing 13.7, 8.4–28.6% of the total population of p-c-Jun+ nuclei (pyramidal and interneuron; Fig. 7*I*).

Together, these data highlight the vulnerability of locally projecting PV+ interneurons to mild cFPI. We found compelling evidence that PV+ interneuron PSAI is not an isolated phenomenon. Rather, PV+ interneuron PSAI comprises almost 70% of all GABAergic DAI and is a significant component of mTBI pathology. Furthermore, p-c-Jun early expression and rapid increase within the PV+ interneuron PSAI population in the absence of neuronal loss provides evidence for acute retrograde genetic responses in the sustaining somas attendant with widespread anterograde axonal terminal loss.

Reduced Inhibitory Transmission within PV+ Interneurons

Our finding of widespread tdTomato+ axonal/terminal debris at 24 h post-mTBI (Fig. 7*C*) prompted us to assess local inhibitory networks for functional disconnection. Whole-cell patch-clamp recordings from tdTomato+ interneurons within S1 layer 5

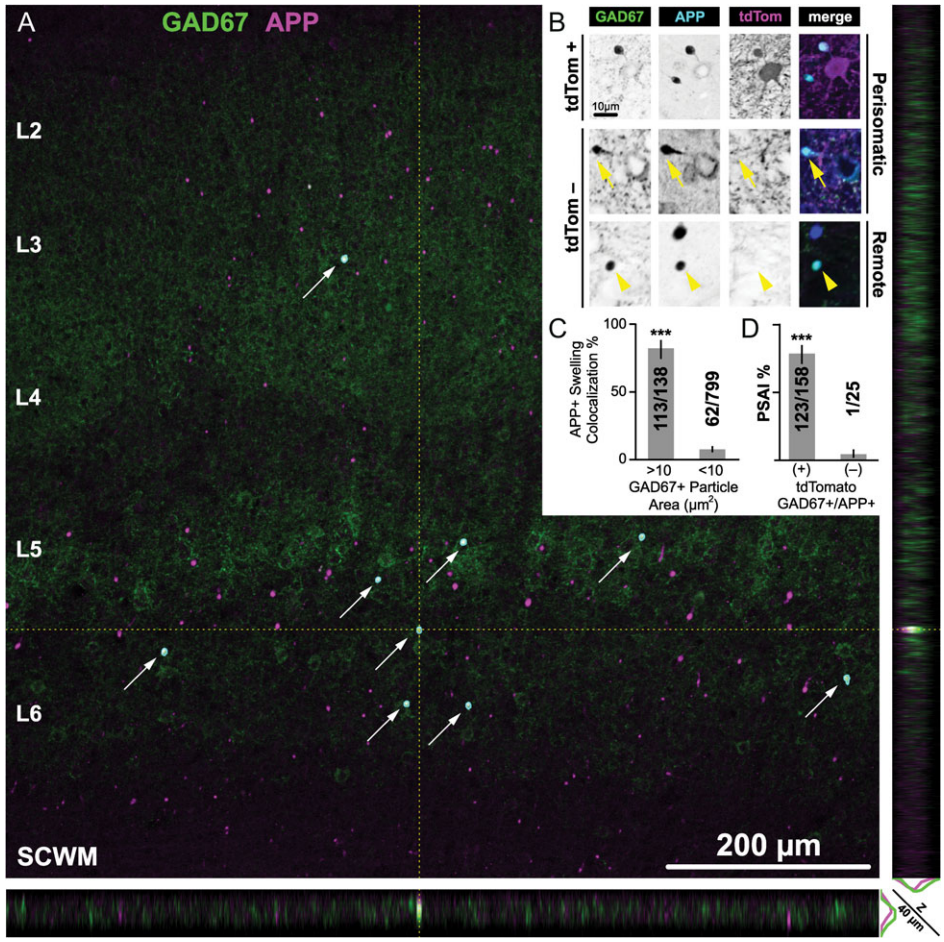

Figure 5. Quantitative analysis of GABAergic DAI at 3 h post-mTBI. (*A*) Representative low-magnification (×10 objective) maximum intensity projection of S1 layers 2–6, with corresponding XZ (bottom) and YZ (right) planes through the center of a GAD67+/APP+ axonal swelling, which can be readily identified visually (arrows) and also using automated image analysis (cyan outlines). Note the scattered distribution of APP+ axonal swellings across the XY plane of S1 layers 2–6 and the sparse distribution of the APP+/GAD67+ subpopulation. XZ and YZ planes highlight GAD67 colocalization with APP is not an artifact of flattening z-stacks. (*B*) Representative higher-magnification (×20 objective) single optical slices through the center of visually identified GAD67+/APP+ axonal swellings. Top and middle panels show tdTomato+ and tdTomato– PSAI (yellow arrow), respectively. Bottom panel shows an isolated/remote tdTomato– axonal swelling (yellow arrowheads). (*C*,*D*) Summary of quantitative data reported as mean percentage with 95% CI error bars. (*C*) GAD67+ accumulations are a positive predictor of APP+ axonal swellings. The proportion of GAD67+ profiles with areas >10 µm^2 that colocalized with APP+ axonal swellings (0.819, 95% CI: 0.746–0.874) was significantly greater (X^2 = 426, ***P < 0.0001) than the proportion of GAD67+ profiles with areas <10 µm^2 (0.078, 95% CI: 0.061–0.98). (*D*) The majority of GABAergic DAI is represented by tdTomato+ PSAI. The proportion of tdTomato+ PSAI (0.779, 95% CI: 0.708–836) was significantly greater (X^2 = 53.9, ***P < 0.0001) than the proportion of tdTomato– axonal injury (0.040, 95% CI 0.007–0.195). Statistics: Chi-squared test used to determine significance. Counts obtained from n = 15 sections from 5 mice.

demonstrated fast-spiking action potentials (Fig. 8A), a physiologic marker of PV+ interneurons (Kawaguchi and Kubota 1997). This included brief action potentials and little adaptation during sustained depolarization. The medians [IQR] of intrinsic properties between sham and mTBI were similar (*F-I* slope [Hz/pA]: sham = 1.0 [0.8–1.4], mTBI = 0.9 [0.7–1.3], X^2 = 1.08, P = 0.2982; Adaptation Ratio: sham = 1.1 [0.9–1.3], mTBI = 1.2 [1.1–1.3], X^2 = 3.69, P = 0.0547; action potential half-width (ms), sham = 0.52 [0.50–0.57], mTBI = 0.55 [0.50–0.69], X^2 = 1.22, P = 0.2691; Wilcoxon test). Considering PV+ interneurons strongly and selectively inhibit one another (Pfeffer et al. 2013) and our observation that the majority of GABAergic DAI is represented by tdTomato+ interneuron PSAI (Fig. 5D), disconnecting the entire distal axonal arbor (Fig. 2F), we expected an alteration of inhibitory transmission at 24 h post-mTBI. We found sIPSC (median, IQR) frequency (Fig. 8E) significantly decreased by 60% in (6.0, 4.0–9.0 Hz) compared with sham (14.5, 10.4–19.4 Hz). The sIPSC amplitude (Fig. 8F) also significantly decreased by 23% (sham = 29.3, 25.5–49.3 mV; mTBI = 22.6, 18.7–30.9 mV). Consistent with an overall reduction of inhibitory input to tdTomato+ interneurons, the sIPSC event area (charge transfer; Fig. 8G) following mTBI (76.3, 60.2–92.6 pA ms) significantly decreased by 32% compared with sham (112.7, 72.6–187.5 pA ms). Collectively, our structural and functional data demonstrate the impact of mTBI on local inhibitory networks embedded within neocortical GM, where reduced inhibitory transmission occurred in concert with PV+ interneuron PSAI and widespread terminal degeneration.

Discussion

This study provides compelling evidence of structural and functional disconnection of local neocortical inhibitory networks via DAI in well-characterized PV-Cre;Ai9 mice after clinically relevant mTBI. Exploiting Cre-driven tdTomato expression in PV+ interneurons coupled with detailed confocal and ultrastructural analysis, we show for the first time that mTBI induces

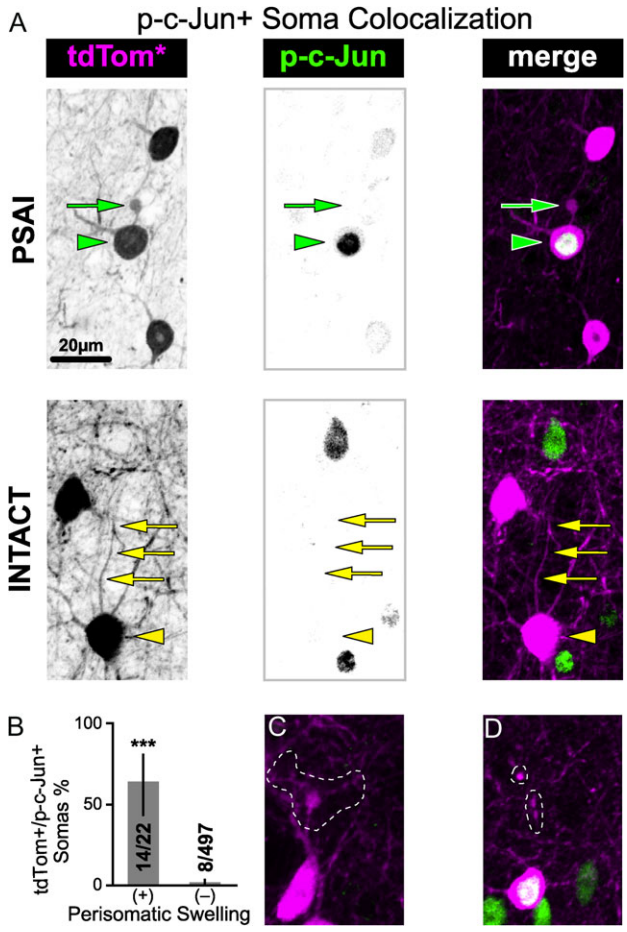

Figure 6. tdTomato+ interneuron PSAI is associated with retrograde nuclear expression of p-c-Jun within 3 h post-mTBI. (*A*) Representative images of 2 distinct tdTomato+ somas within a field of p-c-Jun+ nuclei in S1 layer 5. "TOP," tdTomato+/p-c-Jun+ soma (green arrowhead) contiguous with PSAI (green arrow). "BOTTOM," tdTomato+/p-c-Jun– soma (yellow arrowhead) with an intact axon (yellow arrows). (*B*) Summary data reported as mean percentage with 95% CI error bars. The proportion of tdTomato+/p-c-Jun+ somas with perisomatic swellings (PSAI: 0.636, 95% CI: 0.430–80.3) was significantly greater (***$P < 0.0001$; Fisher's exact test) than the proportion with intact profiles (0.016, 95% CI: 0.008–0.031%). Counts obtained from single sections taken from $n = 5$ mice.

GABAergic interneuron DAI across neocortical layers 2–6. Consistent with human mTBI, midline cFPI reproducibly evoked DAI without mass lesions, neocortical contusion, and/or cell death. Using established markers of impaired axonal transport (APP) and neuronal stress (p-c-Jun) we confirmed DAI within GABAergic interneurons that comprise only a small fraction of neocortical neurons. Further, in this mTBI-mediated response, colocalization of GABAergic and DAI markers revealed a disproportionate involvement of PV+ interneurons and vulnerability for PSAI. Patch-clamp recordings of tdTomato+ fast-spiking interneurons showed reduced inhibitory transmission. Taken together, these findings demonstrate significant structural and functional disconnection of local neocortical inhibitory networks independent of excitatory input from WM tracts. Our results depart from current thought on mTBI, which has been based primarily on the presumption of WM tract vulnerability without any consideration of neocortical involvement. Collectively, the novel neuronal and physiologic substrates identified in this study significantly extend our knowledge of neocortical network dysfunction following mTBI.

Several features of our cFPI model underscore its clinical relevance and utility for evaluating DAI in neocortical networks after mTBI (Lifshitz et al. 2016; McGinn and Povlishock 2016). We used LORR as a surrogate for LOC to assess injury severity (Morehead et al. 1994). The duration of LORR in mice was similar to LOC in humans following mTBI, ranging 3–5 min (Malec et al. 2007). While this was our only behavioral assessment, we monitored arterial oxygen saturation, heart rate, respiratory rate, and core body temperature in all mice used for structural and functional studies. Specifically, all mice were in physiological homeostasis, with no evidence of any mass lesions, neocortical contusion, and/or cell death, a finding entirely consistent with human mTBI (Andriessen et al. 2010; Blyth and Bazarian 2010). Importantly, evaluating these parameters help distinguish our study from most other investigations, which do not perform routine physiologic monitoring to exclude secondary insults that could severely confound the assessment of network disruption via diffuse structural and functional changes. Although other investigations have shown neocortical GABAergic interneuron changes, these were in the context of cell death using models of blunt-force trauma (Carron et al. 2016) or more severe TBI involving mass lesions/contusion (Cantu et al. 2014; Hsieh et al. 2017) to model epileptogenesis (Pitkänen and McIntosh 2006; Hunt et al. 2013), which is not an outcome of clinical or experimental mTBI (Alexander 1995; Shaw 2002; Blyth and Bazarian 2010). Further, while cell death was for many years viewed as the primary contributor to morbidity after TBI, it is now recognized that mTBI pathophysiology conditions ensue without neuronal loss (Farkas and Povlishock 2007).

The markers previously used to understand DAI pathogenesis and its implications for network disconnection had several limitations. Specifically, APP accumulates at focal sites of impaired axonal transport, which can be readily observed in dense WM tracts, but cannot be used to trace long-distance projections back to the soma of origin (Büki et al. 2000). Further complicating this issue is that not all injured axons develop swellings (Stone et al. 2001). Lastly, APP is ubiquitously expressed by neocortical neurons (Bahmanyar et al. 1987) and cannot provide information on the type of fiber system involved (e.g., glutamatergic or GABAergic). Since WM tracts are composed of axons projecting from excitatory pyramidal neurons that represent ~80% of total neocortical neurons (DeFelipe and Fariñas 1992), this has contributed to the long-held misconception that only long-distance fibers are vulnerable to traumatic forces (Adams et al. 1989, 1991). Further complicating this issue is that WM axon density is in the realm of 2 orders of magnitude greater than neocortical GM (Zhang and Sejnowski 2000; Carlo and Stevens 2013; Walhovd et al. 2014). Hence, a disproportionately higher burden DAI based on APP immunoreactivity would be expected. This has not been considered in any studies to date and thus it remains unknown whether DAI vulnerability varies between WM tracts and neocortical GM.

To dissect specific neuronal components of local neocortical network dysfunction, we employed Cre/lox mice to genetically label the total population of PV+ interneurons. As only ~20% of neocortical neurons are GABAergic, we chose to probe PV+ interneurons, which are the largest subclass representing 40–50% of total inhibitory interneurons (Rudy et al. 2011). While Cre/lox mice have become an essential tool for studying neocortical structure and function, caution must be exercised when labeling specific neuronal populations (Taniguchi et al. 2011). In our hands, quantitative analysis showed >90% colocalization between Cre-driven tdTomato expression and endogenous PV immunoreactivity. Thus, PV-Cre;Ai9 animals enabled

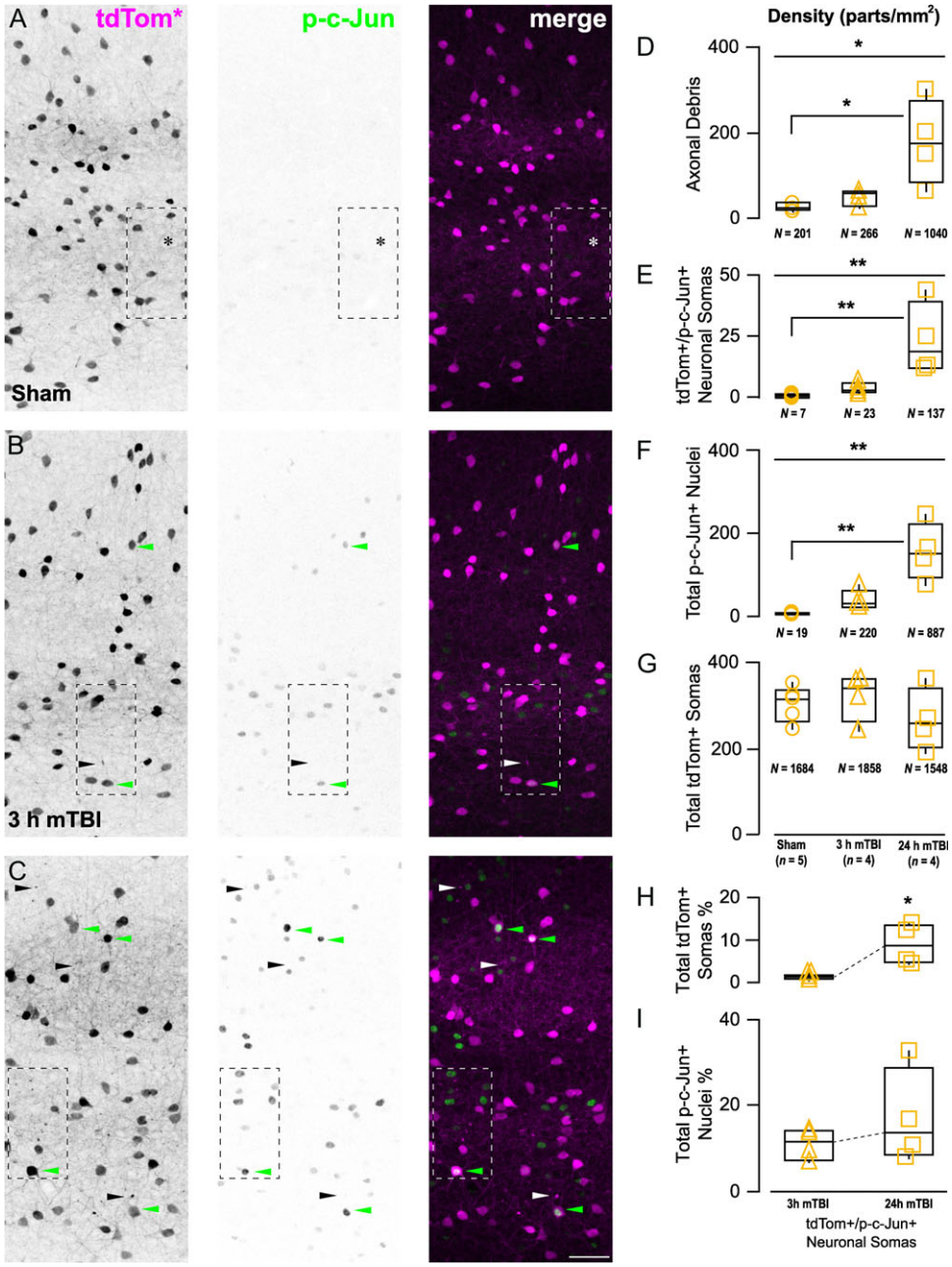

Figure 7. Anterograde axonal degeneration and retrograde p-c-Jun nuclear expression progresses rapidly following mTBI. (*A–C*) Representative maximum intensity projections showing mTBI-induced changes in tdTomato+ profiles and p-c-Jun immunoreactivity across S1 layers 2–6. (*A*) Sham-injury did not induce any tdTomato+ neuropathology and p-c-Jun immunoreactivity was virtually absent. (*B*) Within 3 h post-mTBI tdTomato+ axonal debris (black/white arrowheads) is seen near a tdTomato+/p-c-Jun+ neuronal soma (green arrowhead). (*C*) At 24 h post-mTBI the density of tdTomato+ axonal debris and p-c-Jun+ nuclei increase drastically. (*D–G*) Quantitative data summarized using median, IQR, and min/max values. The density of tdTomato+ axonal debris (*D*), tdTomato+/p-c-Jun+ somas (*E*), and total p-c-Jun+ nuclei (*F*) were significantly different across experimental groups ($X^2_2 = 8.61$, $^*P = 0.0135$; $X^2_2 = 10.5$, $^{**}P = 0.0053$; and $X^2_2 = 10.7$, $^{**}P = 0.0048$, respectively). Post hoc analyses revealed significant increases in at 24 h post-mTBI compared with sham (*D*, tdTomato+ axonal debris: $^*P = 0.0381$; *E*, tdTomato+/p-c-Jun+ somas: $^{**}P = 0.0034$; *F*, total p-c-Jun+ neurons: $^{**}P = 0.0031$). (*G*) tdTomato+ soma density did not change overtime ($P = 0.4401$). *H*, *I*, Overall burden of injury, estimated as percentage of tdTomato+/p-c-Jun+ somas, with respect to total tdTomato+ somas (*H*) significantly increased overtime ($X^2 = 5.33$, $^*P = 0.0209$), while there was no change with respect to total p-c-Jun+ nuclei ($P = 0.3865$). Statistics: Significant differences were determined using Kruskal–Wallis test followed by post hoc pair-wise comparisons using Dunn's method with control (sham) for joint ranking (*D–G*) and Wilcoxon test (*H*, *I*). Each data point (statistical unit) corresponds to a single section per animal (*n*). The total counts per group (*N*) are denoted underneath each graph.

axon identification based on tdTomato+ profiles alone, while also allowing us to follow the same interneuron from confocal to EM via antibodies targeting tdTomato. With confocal microscopy, we routinely identified DAI in a population that represented ≤10% of total neocortical neurons. Ultrastructural analysis of tdTomato+ PSAI revealed vesicle/organelle-laden swellings pathognomonic of impaired axonal transport (Povlishock 1993; Christman et al. 1994). The distal disconnected segment was disorganized indicating rapid onset of Wallerian degeneration (Kelley et al. 2006). To unequivocally demonstrate PV+ interneuron

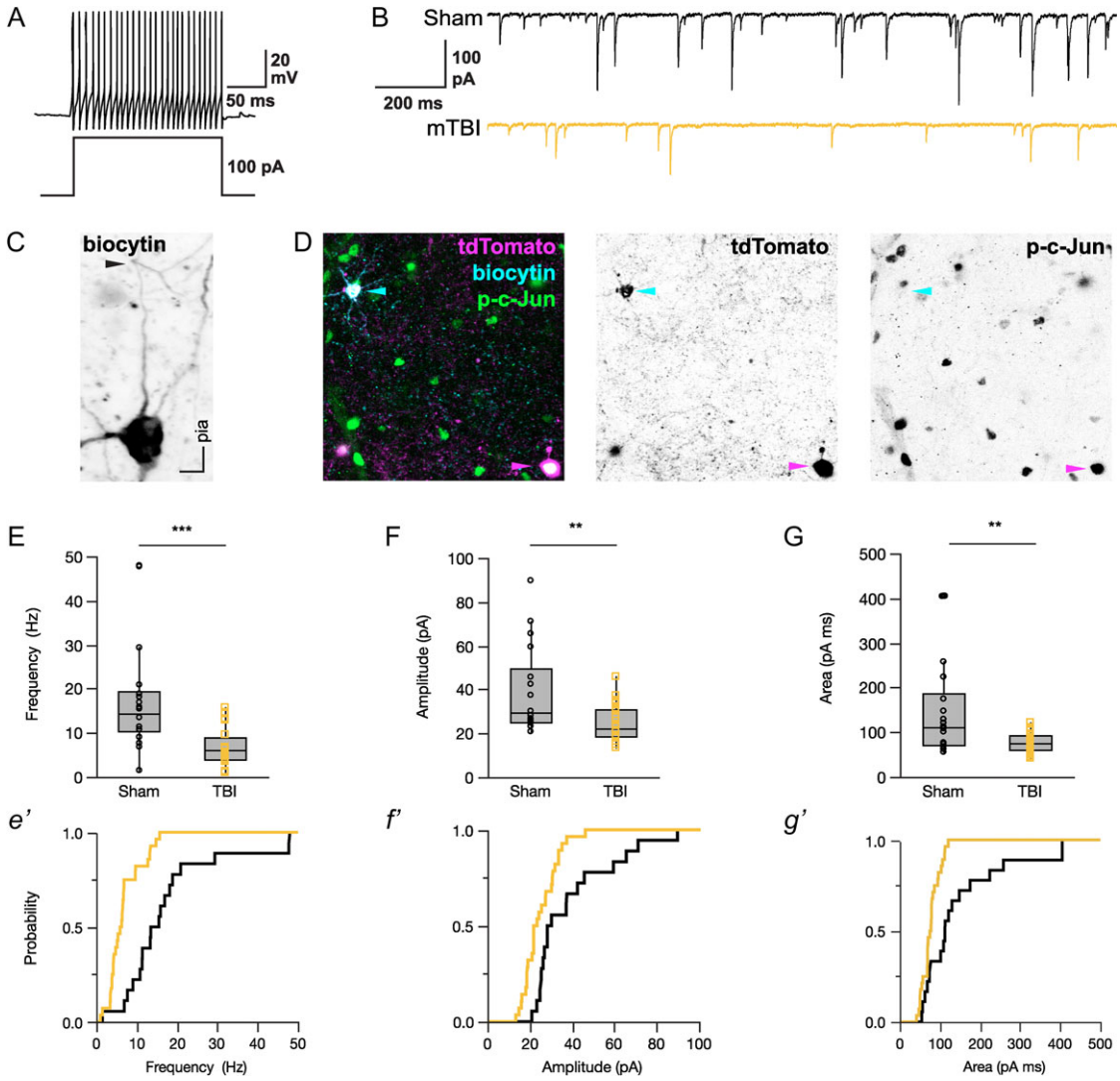

Figure 8. sIPSC is reduced in tdTomato+ fast-spiking interneurons 24 h post-mTBI. (*A*, *B*) Representative traces of whole-cell patch-clamp recordings made in S1BF layer 5 showing fast-spiking action potentials characteristic of PV+ interneurons (*A*), and sIPSCs from sham-injury (black) and mTBI (gold) mice (*B*). (*C*) A representative biocytin-filled tdTomato+ interneuron from a mTBI animal revealing an ascending intact axon that can be continuously traced distally through and past the initial branch point (arrowhead). (*D*) Post hoc confocal image showing a biocytin-filled tdTomato+ interneuron (top left, cyan arrowhead) within a field of diffuse p-c-Jun immunoreactivity (green). Note the tdTomato+/p-c-Jun+ PSAI neuron (bottom right, magenta arrowhead). (*E*–*G*) sIPSC recordings summarized using median, IQR, and min/max values. At 24 h post-mTBI, there was a significant decrease in frequency (*E*, $X^2 = 17.2$, $^{***}P < 0.0001$), amplitude (*F*, $X^2 = 8.56$, $^{**}P = 0.0034$), and event area/charge transfer (*G*, $X^2 = 8.17$, $^{**}P = 0.0043$; *G*) of sIPSC compared with shams. Statistics: Individual tdTomato+ interneurons were considered as the statistical unit (Sham: $n = 18$ from 9 mice; mTBI: $n = 28$ from 12 mice). Significant differences determined using Wilcoxon test.

DAI, we immunolabeled endogenous PV and APP and showed that immunoreactive accumulations of these proteins mapped to tdTomato+ swellings. Similarly, we further confirmed GABAergic DAI by targeting GAD67, which also undergoes fast anterograde transport (Koo et al. 1990; Kanaani et al. 2010) and accumulates within APP+ axonal swellings. Capitalizing on the utility of GAD67 as a reliable DAI marker, we determined that PV+ interneuron DAI represented almost 90% of all GABAergic DAI, suggesting limited involvement of other inhibitory interneuron subclasses. This observed preferential involvement of PV+ interneurons may be due to the "metabolic hypothesis" that postulates that their fast-spiking behavior creates a high-energy demand in both their soma and axonal domains (Kann 2016). Indeed, PV+ interneurons have the highest concentration of axonal mitochondria compared with other neurons (Kann et al. 2014) and local ongoing neocortical activity consumes the majority of brain energy (Buzsáki et al. 2007). The use of GAD67/APP to identify GABAergic DAI also confirmed that the vast majority of tdTomato+ swellings demonstrated PSAI. Previously, we showed that mTBI-induced DAI primarily within the axon initial segment (AIS) of excitatory pyramidal neurons (Greer et al. 2013), where action potentials are generated (Kole and Stuart 2012). The currently observed PV+ interneuron PSAI, together with the previously observed pyramidal AIS involvement, suggests that perisomatic/AIS vulnerability may be a distinguishing neocortical DAI feature (Stone et al. 1999; Farkas and Povlishock 2007). The AIS is a conserved structure with a highly developed subaxolemmal cytoskeleton integrated with a

unique extracellular matrix via cell adhesion molecules (Grubb and Burrone 2010). A recent review (Hemphill et al. 2015) underscores the concept that physical forces are transmitted across all spatial scales (Van Essen 1997) suggesting that the relatively gross tissue deformation used to describe WM tract vulnerability may not account for the forces exerted on the underlying cellular structures in different brain regions. Thus, the perisomatic/AIS domain may represent a structural vulnerable domain on a much finer scale, where mechanotransduction through the neuronal microenvironment may be a potential mechanism underlying neocortical PSAI (Hemphill et al. 2015).

The anterograde and retrograde sequelae of PV+ interneuron PSAI involved both structural and functional changes. In the current study, the observed PV+ interneuron PSAI evolved rapidly following mTBI. Similar to previous findings, by 24 h post-mTBI identifying tdTomato+ PSAI became difficult, likely due to anterograde transport suspension/reversal (Povlishock and Stone 2001). Circumventing this limitation, we used a previously established strategy incorporating p-c-Jun, a nuclear transcription factor (Raivich et al. 2004), as a surrogate DAI marker (Greer et al. 2011; Wang et al. 2013) to spatiotemporally assess retrograde changes in the sustaining somas of origin. Nuclear expression of p-c-Jun increased within 3 h post-mTBI and was consistently associated with tdTomato+ PSAI, thus reaffirming our previous findings and further supporting the use of p-c-Jun as a pan-neuronal DAI marker. Temporal assessment of tdTomato+ profiles also showed a strongly correlated, dramatic increase in anterograde axonal debris and retrograde p-c-Jun expression, thereby supporting their linkages with these anterograde changes most likely reflecting widespread axon terminal degeneration concomitant with deafferentation of target neurons (Erb and Povlishock 1991; Povlishock et al. 1992; Patel et al. 2016). Importantly, this neuropathology evolved without evidence of neuronal loss, consistent with the observation of tdTomato+ interneuron PSAI associated with retrograde p-c-Jun nuclear expression, indicating activation of genetic programs involving cell survival and axonal regeneration (Christman et al. 1997; Raivich et al. 2004; Greer et al. 2011; Wang et al. 2013; Patel et al. 2016). Based on the robust expression of p-c-Jun at 24 h post-mTBI, we determined that ~9% of tdTomato+ interneurons underwent DAI. Previously, we estimated ~5% of Thy1-expressing layer 5 pyramidal neurons undergo DAI (Greer et al. 2011). To the best of our knowledge, these 2 studies are the only quantitative estimates of the proportion of neocortical DAI following experimental mTBI in mice. Further, we estimate that of the total population of p-c-Jun+ population (pyramidal and interneuron DAI), ~14% is accounted by tdTomato+ interneurons. This suggests that ~86% of neural DAI is represented by pyramidal neurons, which is consistent with that fact that this is approximately the same percentage of pyramidal neurons comprising the total neocortical neuron population. Overall, both our qualitative and quantitative data validate that neocortical PV+ interneuron PSAI is not an isolated phenomenon. Rather, it is a consistent and significant component of mTBI-induced pathology, with major functional implications for postsynaptic neurons.

GABAergic interneuron structure reflects function (Hangya et al. 2014; Kepecs and Fishell 2014). Specifically, the expansive axonal arbors of PV+ interneurons highlight their role in balancing neocortical excitation/inhibition to synchronizing neuronal ensembles (Bartos et al. 2007; Buzsáki and Wang 2012; Hu et al. 2014), which play major roles in plasticity and behavior (Kuhlman et al. 2013; Doron et al. 2014). Operationally, the strong and selective connectivity between PV–PV interneurons (Pfeffer et al. 2013) leads to disynaptic disinhibition forming powerful local neocortical networks that generate gamma oscillations during cognition (Howard 2003; Cardin et al. 2009; Sohal et al. 2009). Hence, PV+ interneuron firing is a "pulse" of local excitatory/inhibitory network activity (Scholl et al. 2015; Trachtenberg 2015). Accordingly, the impact of mTBI on local neocortical inhibitory networks via PV+ interneuron PSAI also involved functional disconnection. Applying ionotropic glutamate receptor antagonist pharmacologically isolated local neocortical inhibitory networks from excitatory WM tract (extrinsic) and collateral (intrinsic) inputs. Patch-clamp recordings of tdTomato+ interneurons showed fast-spiking action potentials characteristic of PV+ interneurons (Kawaguchi and Kubota 1997). Importantly, PV+ interneuron intrinsic properties were similar between shams and mTBI. This supported that tdTomato+ interneurons in mTBI slices were healthy, consistent with our observation that ~9% of PV+ interneurons underwent DAI. Notwithstanding this relatively subtle burden of injury, inhibitory transmission in PV+ interneurons was compromised following mTBI, marked by a 60% and 32% decrease in sIPSC frequency and event area (charge transfer), respectively. Such a drastic decrease in inhibitory transmission is consistent with known properties of PV+ interneurons described above and our findings that PSAI disconnects the distal axonal arbor causing widespread axonal degeneration and terminal loss/deafferentation of postsynaptic neurons in local neocortical networks. Since PV+ interneurons strongly inhibit one another via perisomatic innervation (Tamás et al. 2000) and inhibitory presynaptic discharge does not saturate all postsynaptic $GABA_A$ receptors (Perrais and Ropert 2000), this may potential explain the subtle decrease in sIPSC amplitude (Williams and Mitchell 2008). IPSCs play a major role in local (intrinsic) neocortical networks (Hasenstaub et al. 2005), which can operate independent of sensory (extrinsic) inputs via ongoing spontaneous activity (Haider and McCormick 2009; Raichle 2010). In such a scenario local network dysfunction elicited by DAI within neocortical GM could provide a potential mechanism of clinically significant mTBI without WM tract involvement (Zhang et al. 2010; Wäljas et al. 2014). While our electrophysiological assessments were not comprehensive, the paucity of information on the role of GABAergic interneurons in neocortical network dysfunction following mTBI adds importance to our findings and warrants future investigations. Taken together, our electrophysiological findings show that even a small fraction of PV+ interneuron PSAI is enough to cause substantial reduction of GABAergic transmission within local neocortical inhibitory networks following mTBI.

Converging evidence provided by our laboratory and others underscores that TBI involves both excitatory and inhibitory systems (Reeves et al. 1997; Cohen et al. 2007; Cole et al. 2010; Gupta et al. 2012; Guerriero et al. 2015; Beamer et al. 2016). This forces reconceptualization of the anatomical structures vulnerable to DAI and the impact of specific neuronal subtypes on cortical network dysfunction following TBI (Sharp et al. 2014). In an earlier report, we showed ultrastructural evidence of terminal degeneration along the perisomatic domain of pyramidal neurons within layer 5 neocortex, suggesting anterograde synaptic loss following PV+ interneuron PSAI (Singleton et al. 2002). More recently, within this same anatomical locus we also reported hyperexcitability of pyramidal neurons and also the local neocortical network (Greer et al. 2012; Hånell et al. 2015a; Sun and Jacobs 2016). Focusing on PV+ interneurons, the current report's structural and functional data from layer 5 neocortex

corroborates our previous findings and implicates GABAergic loss as a contributor to abnormal excitatory pyramidal neuron activity and local neocortical excitatory/inhibitory imbalance. Similarly, PV+ interneuron PSAI in layers 2/3 and 4 could also implicate altered intracortical and thalamocortical input processing, respectively (Gentet 2012).

In light of converging evidence showing cortical network dysfunction is a preeminent sequelae of mTBI, the structural and functional data provided in this investigation has major implications for both the initial post-traumatic morbidity and any subsequent neuronal reorganization/repair. Although clinical studies indirectly support mTBI-induced neocortical inhibitory network disruption, to the best of our knowledge, the current report provides the only direct evidence of the specific neuronal and physiologic substrates involved. Further, this study dismisses the notion that only axons within WM tracts are susceptible to mTBI forces. Considering the neocortical column as the fundamental computational unit for higher-order information processing, understanding such inhibitory interneuron pathophysiology may be crucial for therapy development from a local network perspective (Douglas and Martin 2004; Bullmore and Sporns 2009; Zhang and Raichle 2010). Ultimately, this study reshapes our knowledge of the cerebral landscape affected by mTBI in both animals and humans.

Funding

National Institutes of Health (grant NS077675).

Notes

The authors thank Carol Davis and Susan Walker for invaluable technical assistance; Anders Hånell, Audrey Lafrenaye, Vishal Patel, and Chris Jurgens for experimental insights; Rory McQuiston for scientific discussions, guidance, and suggestions; and lastly, Scott Henderson and Frances White for sharing their expertise in confocal microscopy, which was performed at the VCU Microscopy Facility, supported, in part, by funding from NIH-NCI Cancer Center Support Grant P30 CA016059. *Conflict of Interest*: None declared.

References

Adams JH, Doyle D, Ford I, Gennarelli TA, Graham DI, McLellan DR. 1989. Diffuse axonal injury in head injury: definition, diagnosis and grading. Histopathology. 15:49–59.

Adams JH, Graham DI, Gennarelli TA, Maxwell WL. 1991. Diffuse axonal injury in non-missile head injury. J Neurol Neurosurg Psychiatry. 54:481–483.

Adams JH, Graham DI, Murray LS, Scott G. 1982. Diffuse axonal injury due to nonmissile head injury in humans: an analysis of 45 cases. Ann Neurol. 12:557–563.

Alexander MP. 1995. Mild traumatic brain injury: pathophysiology, natural history, and clinical management. Neurology. 45:1253–1260.

Andriessen TMJC, Jacobs B, Vos PE. 2010. Clinical characteristics and pathophysiological mechanisms of focal and diffuse traumatic brain injury. J Cell Mol Med. 14:2381–2392.

Aron AR. 2007. The neural basis of inhibition in cognitive control. Neuroscientist. 13:214–228.

Atallah BV, Scanziani M. 2009. Instantaneous modulation of gamma oscillation frequency by balancing excitation with inhibition. Neuron. 62:566–577.

Bahmanyar S, Higgins GA, Goldgaber D, Lewis DA, Morrison JH, Wilson MC, Shankar SK, Gajdusek DC. 1987. Localization of amyloid beta protein messenger RNA in brains from patients with Alzheimer's disease. Science. 237:77–80.

Bartos M, Vida I, Jonas P. 2007. Synaptic mechanisms of synchronized gamma oscillations in inhibitory interneuron networks. Nat Rev Neurosci. 8:45–56.

Bashir S, Vernet M, Yoo W-K, Mizrahi I, Theoret H, Pascual-Leone A. 2012. Changes in cortical plasticity after mild traumatic brain injury. Restor Neurol Neurosci. 30:277–282.

Bazarian JJ, Zhong J, Blyth B, Zhu T, Kavcic V, Peterson D. 2007. Diffusion tensor imaging detects clinically important axonal damage after mild traumatic brain injury: a pilot study. J Neurotrauma. 24:1447–1459.

Beamer M, Tummala SR, Gullotti D, Kopil C, Gorka S, Ted Abel, Bass CRD, Morrison B, Cohen AS, Meaney DF. 2016. Primary blast injury causes cognitive impairments and hippocampal circuit alterations. Exp Neurol. 283:16–28.

Blumbergs PC, Scott G, Manavis J, Wainwright H, Simpson DA, McLean AJ. 1995. Topography of axonal injury as defined by amyloid precursor protein and the sector scoring method in mild and severe closed head injury. J Neurotrauma. 12:565–572.

Blumbergs PC, Scott G, Manavis J, Wainwright H, Simpson DA, McLean AJ. 1994. Staining of amyloid precursor protein to study axonal damage in mild head injury. Lancet (London, England). 344:1055–1056.

Blyth BJ, Bazarian JJ. 2010. Traumatic alterations in consciousness: traumatic brain injury. Emerg Med Clin North Am. 28:571–594.

Bouix S, Pasternak O, Rathi Y, Pelavin PE, Zafonte R, Shenton ME. 2013. Increased gray matter diffusion anisotropy in patients with persistent post-concussive symptoms following mild traumatic brain injury. PLoS One. 8:e66205.

Büki A, Okonkwo DO, Wang KK, Povlishock JT. 2000. Cytochrome c release and caspase activation in traumatic axonal injury. J Neurosci. 20:2825–2834.

Bullmore E, Sporns O. 2009. Complex brain networks: graph theoretical analysis of structural and functional systems. Nat Rev Neurosci. 10:186–198.

Buzsáki G, Kaila K, Raichle M. 2007. Inhibition and brain work. Neuron. 56:771–783.

Buzsáki G, Wang X-J. 2012. Mechanisms of gamma oscillations. Annu Rev Neurosci. 203–225.

Cantu D, Walker K, Andresen L, Taylor-Weiner A, Hampton D, Tesco G, Dulla CG. 2014. Traumatic brain injury increases cortical glutamate network activity by compromising GABAergic control. Cereb Cortex. 25:2306–2320.

Cardin J a, Carlén M, Meletis K, Knoblich U, Zhang F, Deisseroth K, Tsai L-H, Moore CI. 2009. Driving fast-spiking cells induces gamma rhythm and controls sensory responses. Nature. 459:663–667.

Carlo CN, Stevens CF. 2013. Structural uniformity of neocortex, revisited. Proc Natl Acad Sci USA. 110:1488–1493.

Carron SF, Yan EB, Alwis DS, Rajan R. 2016. Differential susceptibility of cortical and subcortical inhibitory neurons and astrocytes in the long term following diffuse traumatic brain injury. J Comp Neurol. 524:3530–3560.

Cassidy JD, Carroll LJ, Peloso PM, Borg J, von Holst H, Holm L, Kraus J, Coronado VG. 2004. Incidence, risk factors and prevention of mild traumatic brain injury: results of the WHO collaborating centre task Force on mild traumatic brain injury. J Rehabil Med. 36:28–60.

CDC. 2003. Report to congress on mild traumatic brain injury in the United States:steps to prevent a serious public health

problem, centers for disease control and prevention, national center for injury prevention and control. Atlanta, GA: Centers for Disease Control and Prevention.

Cesarovic N, Nicholls F, Rettich A, Kronen P, Hässig M, Jirkof P, Arras M. 2010. Isoflurane and sevoflurane provide equally effective anaesthesia in laboratory mice. Lab Anim. 44: 329–336.

Christman CW, Grady MS, Walker SA, Holloway KL, Povlishock JT. 1994. Ultrastructural studies of diffuse axonal injury in humans. J Neurotrauma. 11:173–186.

Christman CW, Salvant JB, Walker SA, Povlishock JT. 1997. Characterization of a prolonged regenerative attempt by diffusely injured axons following traumatic brain injury in adult cat: a light and electron microscopic immunocytochemical study. Acta Neuropathol. 94:329–337.

Cohen AS, Pfister BJ, Schwarzbach E, Grady MS, Goforth PB, Satin LS. 2007. Injury-induced alterations in CNS electrophysiology. Prog Brain Res. 161:143–169.

Cole JT, Mitala M, Kundu S, Verma A, Elkind JA, Djandji D, Wabnitz GH, Deeg J, Bulbuc N, Samstag Y, et al. 2010. Correction for Cole et al., dietary branched chain amino acids ameliorate injury-induced cognitive impairment. Proc Natl Acad Sci. 107:2373–2373.

Crick FH. 1979. Thinking about the brain. Sci Am. 241:219–232.

De Beaumont L, Tremblay S, Poirier J, Lassonde M, Théoret H. 2012. Altered bidirectional plasticity and reduced implicit motor learning in concussed athletes. Cereb Cortex. 22:112–121.

DeFelipe J, Fariñas I. 1992. The pyramidal neuron of the cerebral cortex: morphological and chemical characteristics of the synaptic inputs. Prog Neurobiol. 39:563–607.

Delouche A, Attye A, Heck O, Grand S, Kastler A, Lamalle L, Renard F, Krainik A. 2015. Diffusion MRI: Pitfalls, literature review and future directions of research in mild traumatic brain injury. Eur J Radiol. 85:25–30.

Dixon CE, Lyeth BG, Povlishock JT, Findling RL, Hamm RJ, Marmarou A, Young HF, Hayes RL. 1987. A fluid percussion model of experimental brain injury in the rat. J Neurosurg. 67:110–119.

Dodd AB, Epstein K, Ling JM, Mayer AR. 2014. Diffusion tensor imaging findings in semi-acute mild traumatic brain injury. J Neurotrauma. 31:1235–1248.

Doron G, von Heimendahl M, Schlattmann P, Houweling AR, Brecht M. 2014. Spiking irregularity and frequency modulate the behavioral report of single-neuron stimulation. Neuron. 81:653–663.

Douglas RJ, Martin KAC. 2004. Neuronal circuits of the neocortex. Annu Rev Neurosci. 27:419–451.

Douglas RJ, Martin KAC. 2007. Recurrent neuronal circuits in the neocortex. Curr Biol. 17:R496–R500.

Erb DE, Povlishock JT. 1991. Neuroplasticity following traumatic brain injury: a study of GABAergic terminal loss and recovery in the cat dorsal lateral vestibular nucleus. Exp Brain Res. 83:253–267.

Ewald AJ, Werb Z, Egeblad M. 2011. Monitoring of vital signs for long-term survival of mice under anesthesia. Cold Spring Harb Protoc. pdb.prot5563:174–177.

Fagerholm ED, Hellyer PJ, Scott G, Leech R, Sharp DJ. 2015. Disconnection of network hubs and cognitive impairment after traumatic brain injury. Brain. 138:1696–1709.

Farkas O, Povlishock JT. 2007. Cellular and subcellular change evoked by diffuse traumatic brain injury: a complex web of change extending far beyond focal damage. Prog Brain Res. 161:43–59.

Fish KN, Sweet R a, Lewis DA. 2011. Differential distribution of proteins regulating GABA synthesis and reuptake in axon boutons of subpopulations of cortical interneurons. Cereb Cortex. 21:2450–2460.

Fries P. 2009. Neuronal gamma-band synchronization as a fundamental process in cortical computation. Annu Rev Neurosci. 32:209–224.

Gentet LJ. 2012. Functional diversity of supragranular GABAergic neurons in the barrel cortex. Front Neural Circuits. 6:52.

Gentleman SM, Nash MJ, Sweeting CJ, Graham DI, Roberts GW. 1993. Beta-amyloid precursor protein (beta APP) as a marker for axonal injury after head injury. Neurosci Lett. 160: 139–144.

Greer JE, Hånell A, McGinn MJ, Povlishock JT. 2013. Mild traumatic brain injury in the mouse induces axotomy primarily within the axon initial segment. Acta Neuropathol. 126: 59–74.

Greer JE, McGinn MJ, Povlishock JT. 2011. Diffuse traumatic axonal injury in the mouse induces atrophy, c-jun activation, and axonal outgrowth in the axotomized neuronal population. J Neurosci. 31:5089–5105.

Greer JE, Povlishock JT, Jacobs KM. 2012. Electrophysiological abnormalities in both axotomized and nonaxotomized pyramidal neurons following mild traumatic brain injury. J Neurosci. 32:6682–6687.

Grimm K, Lamont L, Tranquilli W, Greene S, Roberston S. 2015. Veterinary anesthesia and analgesia. 5th ed. New York (NY): John Wiley and Sons.

Grubb MS, Burrone J. 2010. Building and maintaining the axon initial segment. Curr Opin Neurobiol. 20:481–488.

Guerriero RM, Giza CC, Rotenberg A. 2015. Glutamate and GABA imbalance following traumatic brain injury. Curr Neurol Neurosci Rep. 15:27.

Gulyás AI, Megías M, Emri Z, Freund TF. 1999. Total number and ratio of excitatory and inhibitory synapses converging onto single interneurons of different types in the CA1 area of the rat hippocampus. J Neurosci. 19:10082–10097.

Gupta A, Elgammal FS, Proddutur A, Shah S, Santhakumar V. 2012. Decrease in tonic inhibition contributes to increase in dentate semilunar granule cell excitability after brain injury. J Neurosci. 32:2523–2537.

Haider B, McCormick DA. 2009. Rapid neocortical dynamics: cellular and network mechanisms. Neuron. 62:171–189.

Hånell A, Greer JE, Jacobs KM. 2015a. Increased network excitability due to altered synaptic inputs to neocortical layer V intact and axotomized pyramidal neurons after mild traumatic brain injury. J Neurotrauma. 32:1590–1598.

Hånell A, Greer JE, McGinn MJ, Povlishock JT. 2015b. Traumatic brain injury-induced axonal phenotypes react differently to treatment. Acta Neuropathol. 129:317–332.

Hangya B, Pi H-J, Kvitsiani D, Ranade SP, Kepecs A. 2014. From circuit motifs to computations: mapping the behavioral repertoire of cortical interneurons. Curr Opin Neurobiol. 26: 117–124.

Hasenstaub A, Shu Y, Haider B, Kraushaar U, Duque A, McCormick DA. 2005. Inhibitory postsynaptic potentials carry synchronized frequency information in active cortical networks. Neuron. 47:423–435.

Hemphill MA, Dauth S, Yu CJ, Dabiri BE, Parker KK. 2015. Traumatic brain injury and the neuronal microenvironment: a potential role for neuropathological mechanotransduction. Neuron. 85:1177–1192.

Hippenmeyer S, Vrieseling E, Sigrist M, Portmann T, Laengle C, Ladle DR, Arber S. 2005. A developmental switch in the response of DRG neurons to ETS transcription factor signaling. PLoS Biol. 3:e159.

Howard MW. 2003. Gamma oscillations correlate with working memory load in humans. Cereb Cortex. 13:1369–1374.

Hsieh T-H, Lee HHC, Hameed MQ, Pascual-Leone A, Hensch TK, Rotenberg A. 2017. Trajectory of parvalbumin cell impairment and loss of cortical inhibition in traumatic brain injury. Cereb Cortex. 27: 5509–5524.

Hu H, Gan J, Jonas P. 2014. Interneurons. Fast-spiking, parvalbumin^{+} GABAergic interneurons: from cellular design to microcircuit function. Science. 345:1255263.

Huang M-X, Harrington DL, Robb Swan A, Angeles Quinto A, Nichols S, Drake A, Song T, Diwakar M, Huang CW, Risbrough VB, et al. 2016. Resting-state magnetoencephalography reveals different patterns of aberrant functional connectivity in combat-related mild traumatic brain injury. J Neurotrauma. doi:10.1089/neu.2016.4581.

Huang M-X, Theilmann RJ, Robb A, Angeles A, Nichols S, Drake A, D'Andrea J, Levy M, Holland M, Song T, et al. 2009. Integrated imaging approach with MEG and DTI to detect mild traumatic brain injury in military and civilian patients. J Neurotrauma. 26:1213–1226.

Hunt RF, Boychuk JA, Smith BN. 2013. Neural circuit mechanisms of post-traumatic epilepsy. Front Cell Neurosci. 7:89.

Ilvesmäki T, Luoto TM, Hakulinen U, Brander A, Ryymin P, Eskola H, Iverson GL, Ohman J. 2014. Acute mild traumatic brain injury is not associated with white matter change on diffusion tensor imaging. Brain. 137:1876–1882.

Isaacson JS, Scanziani M. 2011. How inhibition shapes cortical activity. Neuron. 72:231–243.

Jiao Y, Sun Z, Lee T, Fusco FR, Kimble TD, Meade CA, Cuthbertson S, Reiner A. 1999. A simple and sensitive antigen retrieval method for free-floating and slide-mounted tissue sections. J Neurosci Methods. 93:149–162.

Johnson VE, Meaney DF, Cullen DK, Smith DH. 2015. Animal models of traumatic brain injury. Handb Clin Neurol. 127: 115–128.

Johnson VE, Stewart W, Smith DH. 2013. Axonal pathology in traumatic brain injury. Exp Neurol. 246:35–43.

Kanaani J, Kolibachuk J, Martinez H, Baekkeskov S. 2010. Two distinct mechanisms target GAD67 to vesicular pathways and presynaptic clusters. J Cell Biol. 190:911–925.

Kann O. 2016. The interneuron energy hypothesis: implications for brain disease. Neurobiol Dis. 90:75–85.

Kann O, Papageorgiou IE, Draguhn A. 2014. Highly energized inhibitory interneurons are a central element for information processing in cortical networks. J Cereb Blood Flow Metab. 34:1270–1282.

Kawaguchi Y, Kubota Y. 1997. GABAergic cell subtypes and their synaptic connections in rat frontal cortex. Cereb Cortex. 7:476–486.

Kelley BJ, Farkas O, Lifshitz J, Povlishock JT. 2006. Traumatic axonal injury in the perisomatic domain triggers ultrarapid secondary axotomy and Wallerian degeneration. Exp Neurol. 198:350–360.

Kepecs A, Fishell G. 2014. Interneuron cell types are fit to function. Nature. 505:318–326.

Kinnunen KM, Greenwood R, Powell JH, Leech R, Hawkins PC, Bonnelle V, Patel MC, Counsell SJ, Sharp DJ. 2011. White matter damage and cognitive impairment after traumatic brain injury. Brain. 134:449–463.

Kobori N, Dash PK. 2006. Reversal of brain injury-induced prefrontal glutamic acid decarboxylase expression and working memory deficits by D1 receptor antagonism. J Neurosci. 26: 4236–4246.

Kole MHP, Stuart GJ. 2012. Signal processing in the axon initial segment. Neuron. 73:235–247.

Koo EH, Sisodia SS, Archer DR, Martin LJ, Weidemann A, Beyreuther K, Fischer P, Masters CL, Price DL. 1990. Precursor of amyloid protein in Alzheimer disease undergoes fast anterograde axonal transport. Proc Natl Acad Sci USA. 87:1561–1565.

Kraus MF, Susmaras T, Caughlin BP, Walker CJ, Sweeney JA, Little DM. 2007. White matter integrity and cognition in chronic traumatic brain injury: a diffusion tensor imaging study. Brain. 130:2508–2519.

Kuhlman SJ, Olivas ND, Tring E, Ikrar T, Xu X, Trachtenberg JT. 2013. A disinhibitory microcircuit initiates critical-period plasticity in the visual cortex. Nature. 501:543–546.

Langlois JA, Rutland-Brown W, Wald MM. 2006. The epidemiology and impact of traumatic brain injury: a brief overview. J Head Trauma Rehabil. 21:375–378.

Lazarus MS, Krishnan K, Huang ZJ. 2015. GAD67 deficiency in parvalbumin interneurons produces deficits in inhibitory transmission and network disinhibition in mouse prefrontal cortex. Cereb Cortex. 25:1290–1296.

Lifshitz J, Rowe RK, Griffiths DR, Evilsizor MN, Thomas TC, Adelson PD, McIntosh TK. 2016. Clinical relevance of midline fluid percussion brain injury: acute deficits, chronic morbidities and the utility of biomarkers. Brain Inj. 30:1–9.

Ling JM, Klimaj S, Toulouse T, Mayer AR. 2013. A prospective study of gray matter abnormalities in mild traumatic brain injury. Neurology. 81:2121–2127.

Logothetis NK. 2008. What we can do and what we cannot do with fMRI. Nature. 453:869–878.

Lorincz A, Nusser Z. 2008. Specificity of immunoreactions: the importance of testing specificity in each method. J Neurosci. 28:9083–9086.

Luo Q, Xu D, Roskos T, Stout J, Kull L, Cheng X, Whitson D, Boomgarden E, Gfeller J, Bucholz RD. 2013. Complexity analysis of resting state magnetoencephalography activity in traumatic brain injury patients. J Neurotrauma. 30: 1702–1709.

Mac Donald CL, Dikranian K, Bayly P, Holtzman D, Brody D. 2007. Diffusion tensor imaging reliably detects experimental traumatic axonal injury and indicates approximate time of injury. J Neurosci. 27:11869–11876.

Mac Donald CL, Johnson AM, Cooper D, Nelson EC, Werner NJ, Shimony JS, Snyder AZ, Raichle ME, Witherow JR, Fang R, et al. 2011. Detection of blast-related traumatic brain injury in U.S. military personnel. N Engl J Med. 364:2091–2100.

Madisen L, Zwingman T a, Sunkin SM, Oh SW, Zariwala H a, Gu H, Ng LL, Palmiter RD, Hawrylycz MJ, Jones AR, et al. 2010. A robust and high-throughput Cre reporting and characterization system for the whole mouse brain. Nat Neurosci. 13:133–140.

Malec JF, Brown AW, Leibson CL, Flaada JT, Mandrekar JN, Diehl NN, Perkins PK. 2007. The Mayo classification system for traumatic brain injury severity. J Neurotrauma. 24: 1417–1424.

Manning CF, Bundros AM, Trimmer JS. 2012. Benefits and pitfalls of secondary antibodies: why choosing the right secondary is of primary importance. PLoS One. 7:e38313.

Mannix R, Meehan WP 3rd, Pascual-Leone A. 2016. Sports-related concussions – media, science and policy. Nat Rev Neurol. 12:486–490.

Markram H, Toledo-Rodriguez M, Wang Y, Gupta A, Silberberg G, Wu C. 2004. Interneurons of the neocortical inhibitory system. Nat Rev Neurosci. 5:793–807.

Marquez de la Plata CD, Garces J, Shokri Kojori E, Grinnan J, Krishnan K, Pidikiti R, Spence J, Devous MD, Moore C, McColl R, et al. 2011. Deficits in functional connectivity of hippocampal and frontal lobe circuits after traumatic axonal injury. Arch Neurol. 68:74–84.

Maxwell WL, Povlishock JT, Graham DL. 1997. A mechanistic analysis of nondisruptive axonal injury: a review. J Neurotrauma. 14:419–440.

Mayer AR, Ling J, Mannell MV, Gasparovic C, Phillips JP, Doezema D, Reichard R, Yeo RA. 2010. A prospective diffusion tensor imaging study in mild traumatic brain injury. Neurology. 74:643–650.

Mayer AR, Mannell MV, Ling J, Gasparovic C, Yeo RA. 2011. Functional connectivity in mild traumatic brain injury. Hum Brain Mapp. 32:1825–1835.

McAllister TW. 1992. Neuropsychiatric sequelae of head injuries. Psychiatr Clin North Am. 15:395–413.

McCormick DA. 2003. Persistent cortical activity: mechanisms of generation and effects on neuronal excitability. Cereb Cortex. 13:1219–1231.

McGinn MJ, Povlishock JT. 2016. Pathophysiology of traumatic brain injury. Neurosurg Clin N Am. 27:397–407.

Mittl RL, Grossman RI, Hiehle JF, Hurst RW, Kauder DR, Gennarelli TA, Alburger GW. 1994. Prevalence of MR evidence of diffuse axonal injury in patients with mild head injury and normal head CT findings. AJNR Am J Neuroradiol. 15:1583–1589.

Morehead M, Bartus RT, Dean RL, Miotke JA, Murphy S, Sall J, Goldman H. 1994. Histopathologic consequences of moderate concussion in an animal model: correlations with duration of unconsciousness. J Neurotrauma. 11:657–667.

Newcombe VFJ, Outtrim JG, Chatfield DA, Manktelow A, Hutchinson PJ, Coles JP, Williams GB, Sahakian BJ, Menon DK. 2011. Parcellating the neuroanatomical basis of impaired decision-making in traumatic brain injury. Brain. 134:759–768.

Packer AM, Yuste R. 2011. Dense, unspecific connectivity of neocortical parvalbumin-positive interneurons: a canonical microcircuit for inhibition. J Neurosci. 31:13260–13271.

Palacios EM, Yuh EL, Chang Y-S, Yue JK, Schnyer DM, Okonkwo DO, Valadka AB, Gordon WA, Maas AIR, Vassar M, et al. 2017. Resting-state functional connectivity alterations associated with six-month outcomes in mild traumatic brain injury. J Neurotrauma. doi:10.1089/neu.2016.4752.

Parikh S, Koch M, Narayan RK. 2007. Traumatic brain injury. Int Anesthesiol Clin. 45:119–135.

Patel VC, Jurgens CWD, Krahe TE, Povlishock JT. 2016. Adaptive reorganization of retinogeniculate axon terminals in dorsal lateral geniculate nucleus following experimental mild traumatic brain injury. Exp Neurol. 289:85–95.

Paterno R, Metheny H, Xiong G, Elkind J, Cohen AS. 2016. Mild traumatic brain injury decreases broadband power in area CA1. J Neurotrauma. 33:1645–1649.

Perrais D, Ropert N. 2000. Altering the concentration of GABA in the synaptic cleft potentiates miniature IPSCs in rat occipital cortex. Eur J Neurosci. 12:400–404.

Pfeffer CK, Xue M, He M, Huang ZJ, Scanziani M. 2013. Inhibition of inhibition in visual cortex: the logic of connections between molecularly distinct interneurons. Nat Neurosci. 16:1068–1076.

Phillips LL, Reeves TM. 2001. Interactive pathology following traumatic brain injury modifies hippocampal plasticity. Restor Neurol Neurosci. 19:213–235.

Pitkänen A, McIntosh TK. 2006. Animal models of post-traumatic epilepsy. J Neurotrauma. 23:241–261.

Povlishock J, Stone J. 2001. Traumatic axonal injury. In: Miller L, Hayes R, Newcomb J, editors. Head trauma: basic, preclinical, and clinical directions. New York: John Wiley & Sons, Inc. p. 281–301.

Povlishock JT. 1993. Pathobiology of traumatically induced axonal injury in animals and man. Ann Emerg Med. 22: 980–986.

Povlishock JT, Becker DP, Cheng CL, Vaughan GW. 1983. Axonal change in minor head injury. J Neuropathol Exp Neurol. 42: 225–242.

Povlishock JT, Christman CW. 1995. The pathobiology of traumatically induced axonal injury in animals and humans: a review of current thoughts. J Neurotrauma. 12:555–564.

Povlishock JT, Erb DE, Astruc J. 1992. Axonal response to traumatic brain injury: reactive axonal change, deafferentation, and neuroplasticity. J Neurotrauma. 9(Suppl 1):S189–S200.

Povlishock JT, Katz DI. 2005. Update of neuropathology and neurological recovery after traumatic brain injury. J Head Trauma Rehabil. 20:76–94.

Raichle ME. 2010. Two views of brain function. Trends Cogn Sci. 14:180–190.

Raivich G, Bohatschek M, Da Costa C, Iwata O, Galiano M, Hristova M, Nateri AS, Makwana M, Riera-Sans L, Wolfer DP, et al. 2004. The AP-1 transcription factor c-Jun is required for efficient axonal regeneration. Neuron. 43:57–67.

Reeves TM, Lyeth BG, Phillips LL, Hamm RJ, Povlishock JT. 1997. The effects of traumatic brain injury on inhibition in the hippocampus and dentate gyrus. Brain Res. 757:119–132.

Rudy B, Fishell G, Lee S, Hjerling-Leffler J. 2011. Three groups of interneurons account for nearly 100% of neocortical GABAergic neurons. Dev Neurobiol. 71:45–61.

Salmond CH, Menon DK, Chatfield DA, Williams GB, Pena A, Sahakian BJ, Pickard JD. 2006. Diffusion tensor imaging in chronic head injury survivors: correlations with learning and memory indices. Neuroimage. 29:117–124.

Scholl B, Pattadkal JJ, Dilly GA, Priebe NJ, Zemelman BV. 2015. Local integration accounts for weak selectivity of mouse neocortical parvalbumin interneurons. Neuron. 87:424–436.

Sharp DJ, Scott G, Leech R. 2014. Network dysfunction after traumatic brain injury. Nat Rev Neurol. 10:156–166.

Shaw NA. 2002. The neurophysiology of concussion. Prog Neurobiol. 67:281–344.

Sherriff F, Bridges L, Sivaloganathan S. 1994. Early detection of axonal injury after human head trauma using immunocytochemistry for beta-amyloid precursor protein. Acta Neuropathol. 87:55–62.

Singleton RH, Zhu J, Stone JR, Povlishock JT. 2002. Traumatically induced axotomy adjacent to the soma does not result in acute neuronal death. J Neurosci. 22:791–802.

Smith DH, Hicks R, Povlishock JT. 2013. Therapy development for diffuse axonal injury. J Neurotrauma. 323:307–323.

Sohal VS, Zhang F, Yizhar O, Deisseroth K. 2009. Parvalbumin neurons and gamma rhythms enhance cortical circuit performance. Nature. 459:698–702.

Somogyi P, Tamás G, Lujan R, Buhl EH. 1998. Salient features of synaptic organisation in the cerebral cortex. Brain Res Brain Res Rev. 26:113–135.

Sponheim SR, McGuire K a, Kang SS, Davenport ND, Aviyente S, Bernat EM, Lim KO. 2011. Evidence of disrupted functional connectivity in the brain after combat-related blast injury. Neuroimage. 54(Suppl 1):S21–S29.

Stone JR, Singleton RH, Povlishock JT. 2000. Antibodies to the C-terminus of the beta-amyloid precursor protein (APP): a site specific marker for the detection of traumatic axonal injury. Brain Res. 871:288–302.

Stone JR, Singleton RH, Povlishock JT. 2001. Intra-axonal neurofilament compaction does not evoke local axonal swelling in all traumatically injured axons. Exp Neurol. 172:320–331.

Stone JR, Walker SA, Povlishock JT. 1999. The visualization of a new class of traumatically injured axons through the use of a modified method of microwave antigen retrieval. Acta Neuropathol. 97:335–345.

Strich SJ. 1956. Diffuse degeneration of the cerebral white matter in severe dementia following head injury. J Neurol Neurosurg Psychiatry. 19:163–185.

Sun J, Jacobs KM. 2016. Knockout of cyclophilin-D provides partial amelioration of intrinsic and synaptic properties altered by mild traumatic brain injury. Front Syst Neurosci. 10:63.

Tamás G, Buhl EH, Lörincz A, Somogyi P. 2000. Proximally targeted GABAergic synapses and gap junctions synchronize cortical interneurons. Nat Neurosci. 3:366–371.

Taniguchi H, He M, Wu P, Kim S, Paik R, Sugino K, Kvitsiani D, Kvitsani D, Fu Y, Lu J, et al. 2011. A resource of Cre driver lines for genetic targeting of GABAergic neurons in cerebral cortex. Neuron. 71:995–1013.

Trachtenberg JT. 2015. Parvalbumin interneurons: all forest, no trees. Neuron. 87:247–248.

Tremblay S, de Beaumont L, Lassonde M, Théoret H. 2011. Evidence for the specificity of intracortical inhibitory dysfunction in asymptomatic concussed athletes. J Neurotrauma. 28:493–502.

van der Horn HJ, Kok JG, de Koning ME, Scheenen ME, Leemans A, Spikman JM, van der Naalt J. 2016. Altered wiring of the human structural connectome in adults with mild traumatic brain injury. J Neurotrauma. doi:10.1089/neu.2016.4659.

Van Essen DC. 1997. A tension-based theory of morphogenesis and compact wiring in the central nervous system. Nature. 385:313–318.

Walhovd KB, Johansen-Berg H, Káradóttir RT. 2014. Unraveling the secrets of white matter–bridging the gap between cellular, animal and human imaging studies. Neuroscience. 276:2–13.

Wäljas M, Lange RT, Hakulinen U, Huhtala H, Dastidar P, Hartikainen K, Öhman J, Iverson GL. 2014. Biopsychosocial outcome after uncomplicated mild traumatic brain injury. J Neurotrauma. 31:108–124.

Wang J, Fox MA, Povlishock JT. 2013. Diffuse traumatic axonal injury in the optic nerve does not elicit retinal ganglion cell loss. J Neuropathol Exp Neurol. 72:768–781.

Wang J, Hamm RJ, Povlishock JT. 2011. Traumatic axonal injury in the optic nerve: evidence for axonal swelling, disconnection, dieback, and reorganization. J Neurotrauma. 28:1185–1198.

Williams SR, Mitchell SJ. 2008. Direct measurement of somatic voltage clamp errors in central neurons. Nat Neurosci. 11:790–798.

Wolf JA, Koch PF. 2016. Disruption of network synchrony and cognitive dysfunction after traumatic brain injury. Front Syst Neurosci. 10:43.

Yizhar O, Fenno LE, Prigge M, Schneider F, Davidson TJ, O'Shea DJ, Sohal VS, Goshen I, Finkelstein J, Paz JT, et al. 2011. Neocortical excitation/inhibition balance in information processing and social dysfunction. Nature. 477:171–178.

Zhang D, Raichle ME. 2010. Disease and the brain's dark energy. Nat Rev Neurol. 6:15–28.

Zhang K, Johnson B, Pennell D, Ray W, Sebastianelli W, Slobounov S. 2010. Are functional deficits in concussed individuals consistent with white matter structural alterations: combined FMRI & DTI study. Exp Brain Res. 204:57–70.

Zhang K, Sejnowski TJ. 2000. A universal scaling law between gray matter and white matter of cerebral cortex. Proc Natl Acad Sci USA. 97:5621–5626.

Zhou F, Chen H, Roper SN. 2009. Balance of inhibitory and excitatory synaptic activity is altered in fast-spiking interneurons in experimental cortical dysplasia. J Neurophysiol. 102:2514–2525.